

# Dynamical ejecta and nucleosynthetic yields from eccentric binary neutron-star mergers

L. Jens Papenfort,<sup>1,\*</sup> Roman Gold,<sup>1</sup> and Luciano Rezzolla<sup>1,2</sup>

<sup>1</sup>*Institut für Theoretische Physik, Johann Wolfgang Goethe-Universität, Max-von-Laue-Straße 1, 60438 Frankfurt, Germany*  
<sup>2</sup>*Frankfurt Institute for Advanced Studies, Ruth-Moufang-Straße 1, 60438 Frankfurt, Germany*

With the recent advent of multi-messenger gravitational-wave astronomy and in anticipation of more sensitive, next-generation gravitational-wave detectors, we investigate the dynamics, gravitational-wave emission, and nucleosynthetic yields of numerous eccentric binary neutron-star mergers having different equations of state. For each equation of state we vary the orbital properties around the threshold of immediate merger, as well as the binary mass ratio. In addition to a study of the gravitational-wave emission including  $f$ -mode oscillations before and after merger, we couple the dynamical ejecta output from the simulations to the nuclear-reaction network code `SkyNet` to compute nucleosynthetic yields and compare to the corresponding results in the case of a quasi-circular merger. We find that the amount and velocity of dynamically ejected material is always much larger than in the quasi-circular case, reaching extreme values of  $M_{\text{ej}} \sim 0.1 M_{\odot}$  and  $v_{\text{ej}}/c \sim 0.75$ . At the same time, the properties of this material are rather insensitive to the details of the orbit, such as pericenter distance or post-encounter apoastron distance. Furthermore, while the composition of the ejected matter depends considerably on the equation of state, the nucleosynthetic yields do not, thus indicating that kilonova signatures could provide information on the orbital properties of dynamically captured neutron-star binaries.

PACS numbers: 04.25.Dm, 04.25.dk, 04.30.Db, 04.40.Dg, 95.30.Lz, 95.30.Sf, 97.60.Jd 97.60.Lf 26.60Kp 26.60Dd

## I. INTRODUCTION

The emission of gravitational waves (GWs) emitted from binary neutron-star systems during inspiral as well as the electromagnetic signals emitted after merger have entered the observational realm with the detection of GW170817 [1, 2]. This event not only signalled the beginning of multimessenger astronomy exploiting gravitational-wave observations but also confirmed the hypothesised link between compact binary mergers and short gamma-ray bursts [3–7]. Numerical simulations of merging neutron stars (see [6, 8] for recent reviews), which now include also the modelling of the kilonova emission from this process [7, 9, 10], together with multimessenger observations, have provided important insight on the maximum mass of neutron stars and on the expected distribution in radii [11–18].

Most work on binary neutron stars has focused on the primordial population where the binaries decouple from their environments at large separation and evolve as a two-body system in isolation. In such a configuration, binary orbits efficiently circularise due to GW emission [19] and therefore eccentricity can be eliminated as a free parameter of the system. The binary sources detected by advanced LIGO (adLIGO) are consistent with a low but finite binary eccentricity of  $e \lesssim 0.1$  when entering the adLIGO frequency range [20–22].

The independent population of dynamically formed binaries bears little resemblance to the primordial population. While in both cases the neutron stars are born in supernova explosions, their orbital characteristics are very different. In astrophysical environments where the stellar density is high, such as globular clusters or galactic cores, the assumptions made in Refs. [19, 23] do not apply. Instead,  $N$ -body effects have to be taken into account to understand typical parameters

and event rates (see [24–26] for recent work). Calculations of event rates for binary mergers are challenging even in the primordial case, mainly because many different physical conditions affect the system throughout its long life and many of the involved processes, such as the common-envelope phase, are complicated; despite impressive efforts [27], the combination of these effects remain poorly understood. In addition to these challenges, event rates in dynamically formed systems also depend on the size of the star cluster, on the binary fraction, as well as on the hardening and evaporation, just to name a few additional complications. As a result, event-rate estimates for dynamically-formed binaries are even more uncertain. Bearing these considerations in mind, the estimated event rates are roughly in the range of  $0.003 - 6 \text{ Gpc}^{-3} \text{ yr}^{-1}$  [28]. It is therefore important to investigate the range out to which such sources can be seen. We focus here on the intrinsic aspects related to the dynamics of the system and GW emission. For the sensitivity and instrumental characteristics of adLIGO the numbers suggest so far that GW detections from eccentric sources are expected to be rare at best. In particular, highly eccentric binary neutron stars are extremely difficult to detect for the detector characteristics of adLIGO [29] mainly due to missing signal power at frequencies around  $\sim 100 \text{ Hz}$  where the detector performs best.

The situation is different for next-generation GW detectors such as the Einstein Telescope (ET) [30, 31] or the Cosmic Explorer (CE) [32]. In this new detector era, substantially higher sensitivities will enable detections from cosmological distances. Apart from the naive gain in observed volume, which already boosts detection rates considerably, signals from redshifts  $z = 3$  (as applicable to ET) or even  $z = 6$  (as applicable to CE) are shifted substantially towards lower frequencies by a factor  $1/(1+z)$ . The technological advances that will accompany these instruments, together with novel concepts to use unstable optomechanical filters to compensate for phase dispersion [33, 34] and thus increase the sensitivities of current interferometers near 2 kHz to levels compa-

\* E-mail: papenfort@th.physik.uni-frankfurt.de

rable to ET, make high-frequency GW signals such as merger waveforms, ringdown and  $f$ -mode oscillations much more detectable. For a combined ET and CE era, 0.1 – 10 eccentric binary neutron-star captures could be detected per year [35].

The detection of and parameter estimation from GWs emitted by eccentric binaries is not only an instrumental issue, but also a challenge from a data analysis and modelling perspective. Past and current searches performed on adLIGO data (see, e.g., [36]) are ill-suited for the sources discussed here and one promising suggestion is to use power-stacking [37] to boost the SNR. If eccentric sources are modeled accurately enough, then eccentric binaries can be seen out to larger distances, and parameters such as chirp mass and sky localisation can be estimated more accurately [38], mostly because the richer structure in eccentric waveforms effectively breaks parameter degeneracies. Therefore, even just one detection of GWs from eccentric binaries offers more scientific opportunities than many quasi-circular binary signals. The rarity of these systems makes them good candidates to explain observed enhancements in heavy neutron-capture elements in individual, peculiar low-metallicity galactic environments [39] (see also [26]). It is therefore important and timely to study such sources to lay the theoretical basis for future observational efforts.

The richer structure of GWs from eccentric binaries ranges from small-amplitude modulations in the GW signal when the binary has also modest eccentricities, to short-term GW bursts emitted during each pericenter passage of the binary, which are then separated by a phase with no significant gravitational radiation, in the case of binaries with large eccentricities. It was first realised in Refs. [40, 41], that in case of binaries containing at least one neutron star, there is an additional effect between the pericenter bursts: Tidal perturbations during pericenter passage can excite stellar  $f$ -mode oscillations with a time-varying quadrupole moment and that themselves act as sources of gravitational radiation (see also [42]). This  $f$ -mode signal can dominate the GW losses away from pericenter. As a consequence, the instantaneous GW frequency transitions from the binary-dominated burst signal over to the star-dominated, constant  $f$ -mode frequency. These  $f$ -mode oscillations drain energy from the orbit, causing a GW phase shift and depend on the internal structure and equation of state (EOS) of the neutron star in a way which is not too different from the post-merger signal (see, e.g., [43–48]).

Initial nonlinear studies employing global hydrodynamical simulations in time-dependent spacetimes of dynamically-formed neutron-star binaries have not only confirmed earlier predictions for and quantified the  $f$ -mode contributions, but have further shown that eccentricity also has substantial consequences for the matter dynamics in the late inspiral, merger and post-merger phase of the system [49–54], giving rise to a much richer phenomenology compared to the quasi-circular case (see also [55] for a study on black hole-neutron-star systems). In studies that feature the formation of a hyper-massive neutron star (HMNS) it was discovered that generically (for all EOSs considered) a one-armed spiral instability occurs, that produces gravitational radiation mainly in the  $\ell = 2, m = 1$  mode [52–54, 56], although this contribution

is much smaller than the one in the traditional  $\ell = 2, m = 2$  mode [57, 58].

Aside from GW emission, the dynamical ejecta of neutron-rich matter and hence nucleosynthetic yields can be expected to be greatly affected by orbital eccentricity [59]. It is therefore important to investigate to what extent nucleosynthesis depends on orbital eccentricity in the context of fast mergers in the early universe [26, 39]. Such differences would lead to different implications for the near-infrared/optical lightcurves emitted from such systems [9, 60, 61].

In this paper we report on the most extensive to date investigation of eccentric binary neutron-star evolutions in full general relativity. We focus on following the ejected mass with tracers, compute the resulting nucleosynthetic yields, analyze the spectrograms of the GWs, and compare our results obtained with two different nuclear EOSs and different mass ratios. We show that the mass outflow from these systems is systematically larger than in the corresponding case of binaries with the same EOS and total mass, but in quasi-circular orbits, reaching extreme values of almost  $0.1 M_{\odot}$  of dynamically ejected material. In fact, even the ejected matter from a single non-merging encounter can easily exceed the ejected mass of an entire quasi-circular inspiral and merger. In addition, the more massive ejecta reach higher maximal velocities and both aspects can have important implications for generating kilonova lightcurves [62]. Despite these striking differences in the ejecta properties when compared to their quasi-circular counterparts, we find that the relative nucleosynthetic yields are rather insensitive to the orbital eccentricity.

We also consider the GW emission from these systems and show that the overall structure of pre-merger GW signals consisting of  $f$ -mode oscillations, that are triggered at the periastron passages accompanied by strong bursts, are rather insensitive to the equation of state. Our findings indicate that the systems under investigation here are detectable out to redshifts as large as  $z \sim 0.5$  for ET and CE, but other plausible, not too dissimilar configurations could be detected out to larger distances. In general, our study points to the fact that longer signals with more cycles and/or multiple bursts are more easily detected than short signals with only a single encounter. Although these mergers are not expected to be very common, we argue that, peculiar factors like low-frequency contributions from  $f$ -modes, cosmological redshift of GW signals, better parameter estimation, and the resulting increased detector volume in the context of future GW detectors have to be factored in when estimating their event rates. A final judgement of the true event rates of such systems therefore awaits further detailed and quantitative study of these aspects.

The plan of the paper is as follows. In Sec. II we recall the mathematical and numerical set-up employed in our simulations, together with our choice of EOS and initial data. In Sec. III we present instead our findings, concentrating on the orbital dynamics (III A), on the mass ejection (III B), on the properties of the dynamical ejecta, (III C), on the  $r$ -process nucleosynthesis (III D), and on the gravitational-wave emission (III E). Finally, Sec. IV contains our conclusions and the prospects of future work.

## II. METHODS

In this section we describe the most important parts composing our numerical setup. This includes the evolution schemes, the initial data and data analysis.

### A. Spacetime evolution

The spacetime evolution is governed by the Einstein field equations

$$R_{\mu\nu} - \frac{1}{2}Rg_{\mu\nu} = 8\pi T_{\mu\nu}, \quad (1)$$

for the four-dimensional metric  $g_{\mu\nu}$ . As usual these equations are cast into a form suitable for a numerical treatment as a Cauchy Initial-Value Problem adopting the standard 3+1 split of spacetime [63, 64]. In this formalism, the metric takes the form

$$ds^2 = -\alpha^2 dt^2 + \gamma_{ij}(dx^i + \beta^i dt)(dx^j + \beta^j dt), \quad (2)$$

with  $\gamma_{ij}$  being the spatial metric induced on each hypersurface of the spacetime foliation,  $\alpha$  the lapse function and  $\beta^i$  the shift vector. Together, they form the spatial hypersurface unit normal vector

$$n^\mu = \frac{1}{\alpha} (1, -\beta^i). \quad (3)$$

Using this representation of a general spacetime, it is possible to decompose the Einstein field equations into spatial and temporal parts. Different choices for the independent variables and the addition of multiples of the constraint equations leads to different formulations that are equivalent in the continuum but have different properties in a numerical simulation with finite temporal and spatial resolution. Here, we employ the CCZ4 formalism [65–67] (see also [68] for a first-order version), for which the starting point is the covariant extension of the Einstein equations

$$8\pi \left( T_{\mu\nu} - \frac{1}{2}g_{\mu\nu}T \right) = R_{\mu\nu} + 2\nabla_{(\mu}Z_{\nu)} + \kappa_1 [2n_{(\mu}Z_{\nu)} - (1 + \kappa_2)g_{\mu\nu}n_\sigma Z^\sigma], \quad (4)$$

also known as the Z4 formulation [69–71], where the four-vector  $Z_\mu$  consists of the four constraint equations given by projections of Eq. (1). These constraints have to be fulfilled by any solution of Eqs. (1) and in particular by the initial data for the time integration, so if

$$Z_\mu = 0, \quad (5)$$

the Einstein field equations are recovered. This equivalence in the continuum limit implies that solutions to Eq. (4) under the constraint (5) are also solutions to Eqs. (1), but the two formulations have distinct principal parts and hence different mathematical properties on the continuum level, some

of which carry over to a numerical discretization of Eq. (4). The additional terms involving the constraint-damping coefficients  $\kappa_1$  and  $\kappa_2$  lead to an exponential damping of the constraint violations on a characteristic timescale proportional to the coefficients, which is similar to the divergence cleaning approach in magnetohydrodynamics [72]. While constraint-violation damping is a distinguishing feature of the CCZ4 formulation, it is especially valuable for the approximate initial data used in this study, whose initial violations are large and need to be reduced rapidly (see Sec. IID). In addition, even in the zero damping case, i.e.,  $\kappa_1 = \kappa_2 = 0$ , Z4-based formulations feature a *propagating* mode associated with the Hamiltonian constraint violations as opposed to the classic BSSNOK formulation [73, 74], where a “zero-speed” mode leads to local build-up of Hamiltonian constraint violations due to numerical error. In Z4-based formulations such violations propagate and therefore have a chance to leave the grid. It is therefore expected that Z4-based formulations, which have intrinsically smaller violations of the constraints, yield more accurate spacetime evolutions than the BSSNOK system.

The evolution of the gauge conditions, i.e., lapse and shift, is governed by standard 1+log slicing condition and a Gamma driver (see e.g., [63, 64, 75]). For the numerical solution of the Einstein equations we make use of the publicly available McLachlan code [76] which implements the above evolution equations with fourth-order central finite-difference methods and is part of the Einstein Toolkit [77]. The nonlinear stability of the spacetime evolution is ensured by adding an artificial Kreiss-Oliger dissipation [78] to the spacetime variables.

### B. General-relativistic hydrodynamics

The neutron stars are modeled via a relativistic perfect-fluid energy-momentum tensor [64]

$$T_{\mu\nu} = \rho h u_\mu u_\nu + p g_{\mu\nu}, \quad (6)$$

where  $u^\mu$  is the four-velocity,  $\rho$  the rest-mass density,  $h$  the specific enthalpy, and  $p$  the pressure of the fluid. The relativistic hydrodynamic equations can be derived by means of the Bianchi identity of the Einstein equations (1) giving the local conservation law for the energy-momentum tensor

$$\nabla_\mu T^{\mu\nu} = 0, \quad (7)$$

while the conservation of rest mass is imposed via the continuity equation

$$\nabla_\mu (\rho u^\mu) = 0. \quad (8)$$

The relativistic-hydrodynamic equations (7) and (8) are closed by a suitable EOS expressing the pressure in terms of other thermodynamical variables of the fluid and that we will discuss in more detail in Sec. IIE.

These equations can be cast into conservative form, which is also known as the “Valencia formulation” [79]

$$\partial_t \mathbf{U} + \partial_i \mathbf{F}^i = \mathbf{S}, \quad (9)$$

with the conserved variables  $U$ , the fluxes  $F^i$  and the sources  $S$  depend on the primitive hydrodynamic variables as well as the geometry of the spatial hypersurfaces (see, e.g., [64] for the explicit form of  $U$ ,  $F^i$  and  $S$ ).

These conservation equations are implemented in the `WhiskyTHC` code [80–82], which uses either finite-volume or high-order finite-differencing high-resolution shock-capturing methods.

In these simulations we make use of a particular combination of the finite-volume scheme, the high-order MP5 primitive reconstruction [83, 84], the second-order HLLC Riemann solver [85], the positivity preserving limiter of Refs. [81, 86], and, additionally, refluxing at the refinement boundaries to further improve mass conservation [87]. Finally, as standard in this type of approaches [64], in order to accurately track regions that transition from the fluid to the vacuum regime, all simulations have an artificial low-density background atmosphere which is evolved as discussed in [81]. For all simulations presented in this study we choose an atmosphere value of  $\rho_{\text{atmo}} \sim 6 \times 10^3 \text{ g cm}^{-3}$ , which is therefore of about 11 orders of magnitude smaller than the maximum rest-mass density in the simulations.

### C. Neutrino losses

Neutrino emission is modeled by a grey (i.e., frequency-independent) neutrino leakage scheme (see, e.g., [88–92]). In this scheme the trapped neutrinos do not individually contribute to the energy-momentum tensor itself, however the radiative losses by the non-trapped neutrinos are modeled by a source term to the local conservation law (7) and lepton number  $n_e$  conservation leading to modified conservation equations defined by

$$\nabla_{\mu} T^{\mu\nu} = \Psi^{\nu}, \quad (10)$$

$$\nabla_{\mu} (n_e u^{\mu}) = R, \quad (11)$$

together with Eq. (8). Assuming that the neutrinos are in local thermodynamic equilibrium with the baryonic matter, energy-averaged approximations to the source terms  $\Psi^{\nu}$  and  $R$  are computed. The details of this procedure have been described in [59, 93].

### D. Initial data

We construct our binary neutron-star models as marginally unbound systems by superposing two boosted nonrotating stellar solutions (TOV). The initial separation is fixed to  $100 M_{\odot} \approx 150 \text{ km}$  and we choose the gravitational mass at infinity of the first star to be  $M_1 = 1.35 M_{\odot}$ , while the mass of the second star is set to be  $M_2 = q M_1$ , with  $q \leq 1$  the mass ratio. Further fixing the periastron separation  $r_p$  and assuming that the stars are on a Newtonian parabolic orbit, i.e., the eccentricity is maximal ( $e = 1$ ), determines the initial velocities used for boosting the two TOV solutions. The properties of the models under consideration are listed in Table I.

We should note that this initial data is not constraint satisfying, but approximates the correct initial data as the initial binary separation goes to infinity. This is why the initial coordinate separation is chosen to be much larger than for quasi-circular binaries and we make extensive use of the constraint violation damping provided by the CCZ4 formalism. Confidence on the robustness of our initial data also comes from similar experience developed when an intrinsic spin angular momentum was added to binaries in quasi-circular orbits [94], which produced results very similar when compared to those obtained with a consistent calculation of spinning binaries [95]. We note that the approximate nature of our initial data does not cause any significant GW emission arising from spuriously triggered, (mainly radial) oscillations in the stars. Such oscillations were observed in an earlier work [50], which was later refined with better initial data [51–54] that reproduced the same qualitative physics with respect to the  $f$ -mode oscillations. This agreement further supports the point that the initial data used here, while being only approximate, does incorporate the essential physics to model these systems.

### E. Equations of state

To model the neutron-star matter realistically we employ two different tabulated nuclear EOSs with full composition and temperature dependence, namely DD2 [96] and LS220 [97], where the latter is used with a nuclear compressibility parameter of  $K = 220 \text{ MeV}$ , which makes it softer than the DD2 EOS. Both of these EOSs can support a neutron star of mass  $\sim 2 M_{\odot}$  as required by pulsar observations [98, 99] and have a maximum mass which is in agreement with the most recent estimates [13, 15–17]. The combined use of these EOSs serves us to crudely probe the overall range of possibilities of composition and temperature-dependent EOSs.

We note that recent work in [100] has found the LS220 EOS (together with other EOSs) to violate conservative constraints on the symmetry energy, disfavoring this EOS. Nonetheless, we employ this EOS as a fiducial reference to previous binary neutron-star merger studies, which have made extensive use of this EOS, especially in the case of eccentric mergers [57]. The neutron-star matter is initially setup in beta equilibrium at the minimal temperature of the EOS tables ( $T = 0.01 \text{ MeV}$ ), where the neutrino chemical potential  $\mu_{\nu}$  vanishes. In turn, this equilibrium fixes the initial electron (or equivalently proton) fraction  $Y_e$  distribution in the stars.

### F. Grid setup

The numerical grid is managed by the mesh-refinement driver `Carpet` [101]. It implements a nonuniform grid via a nested set of movable boxes (box-in-box) together with a hierarchical (Berger-Oliger-style) timestepping. In these simulations we employ six refinement levels where each additional level doubles the resolution of the enclosing one. On the finest grid, which is separately centered around each neutron star, the resolution in each dimension is  $\Delta x = 0.15 M_{\odot} \approx 220 \text{ m}$ .

Model	EOS	$r_p$ [ $M_\odot$ ]	$q$	$M_1$ [ $M_\odot$ ]	$M_2$ [ $M_\odot$ ]	$R_1$ [km]	$R_2$ [km]	$M_{b,1}$ [ $M_\odot$ ]	$M_{b,2}$ [ $M_\odot$ ]	$C_1$	$C_2$
LS220-RP11.250	LS220	11.250	1.0	1.35	1.35	12.78	12.78	1.47	1.47	0.156	0.156
LS220-RP12.500	LS220	12.500	1.0	1.35	1.35	12.78	12.78	1.47	1.47	0.156	0.156
LS220-RP13.000	LS220	13.000	1.0	1.35	1.35	12.78	12.78	1.47	1.47	0.156	0.156
LS220-RP13.250	LS220	13.250	1.0	1.35	1.35	12.78	12.78	1.47	1.47	0.156	0.156
LS220-RP13.340	LS220	13.340	1.0	1.35	1.35	12.78	12.78	1.47	1.47	0.156	0.156
LS220-RP13.375	LS220	13.375	1.0	1.35	1.35	12.78	12.78	1.47	1.47	0.156	0.156
LS220-RP11.250-q09	LS220	11.250	0.9	1.35	1.22	12.78	12.85	1.47	1.31	0.156	0.14
LS220-RP12.500-q09	LS220	12.500	0.9	1.35	1.22	12.78	12.85	1.47	1.31	0.156	0.14
LS220-RP13.000-q09	LS220	13.000	0.9	1.35	1.22	12.78	12.85	1.47	1.31	0.156	0.14
DD2-RP11.250	DD2	11.250	1.0	1.35	1.35	13.23	13.23	1.47	1.47	0.151	0.151
DD2-RP12.500	DD2	12.500	1.0	1.35	1.35	13.23	13.23	1.47	1.47	0.151	0.151
DD2-RP13.000	DD2	13.000	1.0	1.35	1.35	13.23	13.23	1.47	1.47	0.151	0.151
DD2-RP13.250	DD2	13.250	1.0	1.35	1.35	13.23	13.23	1.47	1.47	0.151	0.151
DD2-RP13.375	DD2	13.375	1.0	1.35	1.35	13.23	13.23	1.47	1.47	0.151	0.151
DD2-RP14.000	DD2	14.000	1.0	1.35	1.35	13.23	13.23	1.47	1.47	0.151	0.151
DD2-RP11.250-q09	DD2	11.250	0.9	1.35	1.22	13.23	13.19	1.47	1.31	0.151	0.136
DD2-RP12.500-q09	DD2	12.500	0.9	1.35	1.22	13.23	13.19	1.47	1.31	0.151	0.136
DD2-RP13.000-q09	DD2	13.000	0.9	1.35	1.22	13.23	13.19	1.47	1.31	0.151	0.136
DD2-RP14.000-q09	DD2	14.000	0.9	1.35	1.22	13.23	13.19	1.47	1.31	0.151	0.136

TABLE I. Summary of the eccentric binary systems under consideration. Listed are the Newtonian periastron distance  $r_p$ , the mass ratio  $q := M_2/M_1$ , the ADM masses  $M_{1,2}$ , the TOV radii  $R_{1,2}$ , the baryon masses  $M_{b,1,2}$  and the compactness  $C_{1,2} := M_{1,2}/R_{1,2}$ .

The physical domain extends to  $512M_\odot \approx 750$  km, where we track and measure the ejected material. We make explicit use of the reflection symmetry relative to the  $z = 0$  plane to reduce the computational cost essentially without introducing more approximations. The timestep is fixed to 1/6 of the grid spacing, corresponding to a Courant-Friedrichs-Lewy (CFL) factor of 0.15 and a third-order strong stability preserving Runge-Kutta method is used for advancing the computation in time.

We note that we have performed a simulation of model LS220-RP13.25 with a higher resolution of  $\Delta x = 0.1 M_\odot$ , finding overall consistency with the results obtained with our reference resolution of  $\Delta x = 0.15 M_\odot$ . More specifically, in the high-resolution binary we observe that the apoastron separation increases by 4%, showing a slightly different orbital configuration after the first periastron passage. While the overall waveform shows the same qualitative features and amplitudes, the ejected mass is increased by approximately 30%. This is not particularly surprising since the dynamics of the system depends sensitively on the choice made for the impact parameter  $r_p$ .

We also note that while these studies are far from being a systematic convergence analysis, they serve our scope. In fact, the variance introduced because of the finite numerical accuracy – which causes a slight drift on the dependence on  $r_p$  in the parameter space – is compensated by the fact that  $r_p$  is treated here as a free parameter and investigated over a large range. Hence, while the results for a given value of  $r_p$  may not be accurate, the overall dependence of the results on  $r_p$  is.

## G. Analysis methods

### 1. Outflow properties

To measure the properties of the ejected material, we place multiple spherical detectors at different radii around the origin. As a trade-off between resolution and distance from the merger remnant, we take the detector of  $200M_\odot \approx 300$  km coordinate radius for all measurements. Since not all material crossing this surface is unbound, we have to set a physically motivated threshold. Here we use the so called “geodesic criterion”, which is an approximate threshold based on the Newtonian limit, which gets more accurate far away from the strong gravity region

$$u_t \leq -1, \quad (12)$$

where  $\mathbf{u}$  is the fluid four-velocity vector. For a discussion of the effect of this and alternative criteria on the measurements, see, e.g., [102, 103].

### 2. Tracers and nuclear-reaction networks

We employ test-particle tracers which are passively advected along with the fluid, i.e.,

$$\frac{d\vec{x}}{dt} = \vec{v} = \alpha\mathbf{u} + \beta, \quad (13)$$

where  $\vec{x}$  and  $\vec{v}$  are the fluid element’s spatial position and its three-velocity, respectively [103–106].

Two sets of tracers are initialised throughout the simulations. The first set of tracers is initialised at the first encounter, where the separation of the two neutron-star cores is minimal, i.e., at periastron. The second set is initialised once the neutron stars reach their maximum separation so as to be able to track the material of the full tidal arms which develop up to the point of merger. The tracers are placed on the finest refinement level and are sampled uniformly over the whole density range, since it best reproduces the behaviour of the ejected matter (see [103] for a detailed discussion). Some of the lowest density regions are excluded to avoid any oversampling at the boundaries of the finest refinement level. During the evolution the tracers are updated according to the interpolated values of the fluid properties at the location of the tracers.

The thermodynamic trajectories of the unbound set of tracers are subsequently used as input for the `SKYNET` nuclear-reaction network [107]. In section III D we describe which subset of the unbound tracers is used to compute the total r-processed material. Such yields are computed using the most recent JINA REACLIB strong interaction rates [108], neutron-induced fission rates with zero emitted neutrons from Ref. [109] and spontaneous fission rates with zero emitted neutrons calculated in Ref. [110]. Furthermore, we use a combination of the rates from [111] and JINA REACLIB [108] for the weak interactions.

The tracer trajectories are trimmed to begin once their temperatures drop below  $8 \times 10^6$  K and end before their densities drop to near-atmosphere values, or if the fluid element reaches the outer boundary. From there on, we assume a spherical, free expansion of the material, leading to the subsequent extrapolations beginning after the last available data of the tracer trajectory [112, 113]

$$r(t) = r_0 + v_0 t, \quad (14)$$

$$\rho(t) = \rho_0 \left( \frac{t}{t_0} \right)^{-3}, \quad (15)$$

$$T(t) = T[s, \rho(t), Y_e(t)]. \quad (16)$$

where the temperature is computed from the modified Helmholtz EOS implemented in `SKYNET` (see [107, 114, 115] for details). The temperature threshold for the transition from nuclear statistical equilibrium (NSE) to the full nuclear network is assumed to be at  $T = 7$  GK and the r-process is followed up to  $\sim 3 \times 10^6$  yr after merger. This setup is rather standard and similar to the one employed in Ref. [9], where a different nuclear-reaction network code (`WINNET`) was used.

### 3. Gravitational-wave signals

The GW strain is extracted using the standard Newman-Penrose formalism [116], in which a particular contraction of the Weyl tensor with a suitably chosen null tetrad yields a gauge-invariant scalar quantity  $\psi_4$  that encodes the outgoing gravitational radiation (see e.g., [117]). More specifically,  $\psi_4$  is related to the second time derivative of the two strain polarisations  $\ddot{h}_{+, \times}$  by

$$\ddot{h}_{+} - i\ddot{h}_{\times} = \psi_4 = \sum_{\ell=2}^{\infty} \sum_{m=-\ell}^{\ell} \psi_4^{\ell m} {}_{-2}Y_{\ell m}(\theta, \varphi), \quad (17)$$

where we introduced also the multipole expansion of  $\psi_4$  in spin-weighted spherical harmonics [118] of spin-weight  $s = -2$ . In addition, we compute the radiated energy and angular momentum from the radiated torque as

$$j = \frac{r^2}{16\pi} \Im \left( \sum_{\ell=2}^{\infty} \sum_{m=-\ell}^{\ell} m \int_{-\infty}^t \int_{-\infty}^{t'} \bar{\psi}_4^{\ell m} dt' dt' \int_{-\infty}^t \psi_4^{\ell m} dt' \right), \quad (18)$$

and the radiated power as

$$\dot{E} = \frac{1}{16\pi} \sum_{\ell=2}^{\infty} \sum_{m=-\ell}^{\ell} \int_{-\infty}^t |r \psi_4^{\ell m} dt'|^2. \quad (19)$$

The double integrations in time introduce substantial non-linear drifts of the strain as well as of the total radiated angular momentum and energy. To eliminate this artificial drift coming from random numerical noise in the  $\psi_4$  data, we perform all time integrations using the fixed-frequency integration from Ref. [119].

We define the power spectral density (PSD) of the effective strain amplitude as

$$\tilde{h}(f) := \sqrt{\frac{|\tilde{h}_{+}|^2 + |\tilde{h}_{\times}|^2}{2}}, \quad (20)$$

with

$$\tilde{h}(f)_{+, \times} = \begin{cases} \int h_{+, \times}(t) e^{-i2\pi f t} dt & f \geq 0 \\ 0 & f < 0. \end{cases} \quad (21)$$

Note, that the PSD is most informative for signals with well-separated features or with secular variations in frequency, such as for quasi-circular sources. On the other hand, for eccentric sources the instantaneous GW frequency is not a monotonic function of time and signal power in a certain frequency range can overlap in frequency space despite being well-separated in time. The GW spectrograms (cf. Fig. 9) are a much more faithful representation of how the signal manifests itself in the detector (for either quasi-circular or eccentric sources).

## III. RESULTS

### A. Orbital dynamics

Highly eccentric binary mergers exhibit richer dynamics and phenomenology when compared to quasi-circular mergers and more parameters are needed to fully describe the orbital dynamics in its general form. This is shown in Fig. 1,

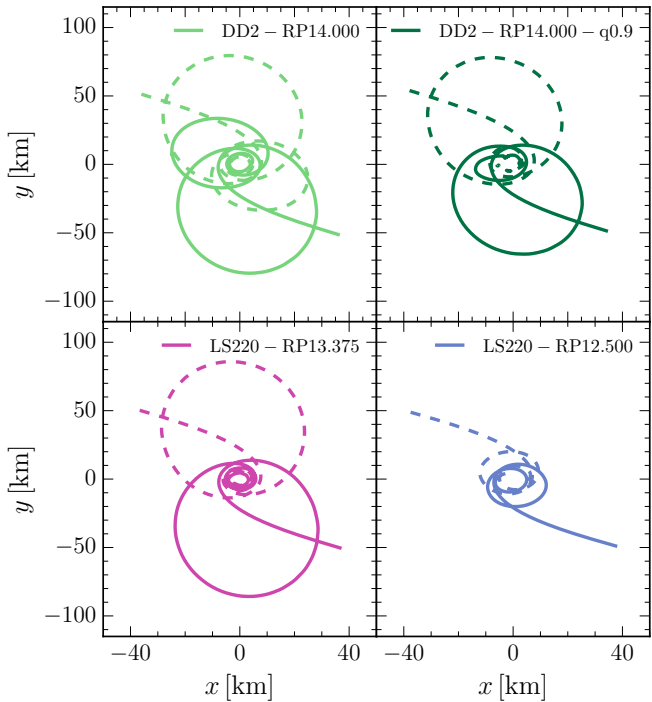


FIG. 1. Orbital trajectories of the barycenters of the neutron stars for four representative models, spanning a large range in periastron values, mass ratio and EOS. Note that some binaries have multiple periastron approaches (e.g., DD2-RP14.000) and that solid/dashed lines refer to the trajectories of either member of the binary.

which reports the orbital trajectories of the barycenters<sup>1</sup> of the neutron stars for four representative models, spanning the set considered in initial periastron distance, mass ratio and EOS. Note that some binaries in our set have multiple (up to three) periastron approaches, i.e., DD2-RP14.000; furthermore, the location of the apoastron can be very large for “bare” captures, i.e., LS220-RP13.375, or very small i.e., DD2-RP12.500.

The systems under consideration here are all setup in a marginally bound orbit with maximum Newtonian eccentricity  $e = 1$ , and with varying periastron separation  $r_p$ . This restriction to a one-dimensional parameter space expressed in terms of a Newtonian description allows us to probe tidal interactions of vastly different strength that are similar to dynamical-capture scenarios that can occur in the cores of globular clusters [120, 121] or in stellar cusps in galactic cores [122–124]. Note however that because of GW losses, all orbits in this study are actually bound, either in the sense that they merge on the first encounter or lose sufficient orbital energy through tides and GW emission that they move apart only up to a finite apoastron distance before returning for the next encounter.

These post-capture apoastron distances increase monotonically with increasing periastron separation because gravita-

tional radiation and the tidal interactions become weaker. This is shown in Fig. 2, where we report the proper separation between the barycenters,  $d_{\text{orb}}$ , for several of the binaries considered here. By comparing cases with the same initial  $r_p$  but different EOSs, it is possible to see clearly that the EOS leads to substantially different orbital dynamics. These differences arise from the interactions of the stars with the binary tidal field, which depends on the EOS. From Fig. 2 it is also possible to deduce that as the initial impact parameter  $r_p$  is increased, the separation after the first periastron passage increases, with binaries that either merge with the second periastron passage (this is the large majority of the cases considered here), or that fly off for yet another orbit. This is indeed the case of the binary DD2-RP14.000, which has a periastron parameter of  $r_p = 14.0 M_\odot$  and undergoes two close passages and merges at the third. Overall, the examples collected in Fig. 2 clearly show that the orbital dynamics for our binaries is only very poorly described by a simplified test-particle approximation, be it in Newtonian gravity or in terms of a geodesic motion in a stationary spacetime in general relativity. In practice, finite-size effects, tidal interactions and GW losses make the dynamics of the system far more complex and accurately described only in terms of fully nonlinear numerical simulations.

We should note that although the pre-merger evolution of the binary DD2-RP14.000 in Fig. 2 extends only to a time  $\sim 17$  ms, the computational costs associated with this binary are indeed extremely high. This is because the grid structure that needs to be employed for a proper analysis of the two stars as they move away from each other requires high-resolution refinement boxes that are very extended and hence computationally expensive. As a reference, the computational costs of the binary DD2-RP14.000 for a timescale of 17 ms would correspond to a post-merger evolution of  $\sim 25$  ms for the same binary merging from a quasi-circular orbit.

Note that all remnants formed in this study are HMNSs, i.e., their mass exceeds the maximum mass of a uniformly rotating neutron star supported by the given EOS  $M_{\text{max}}$ , which is then related in a quasi-universal manner to the maximum mass of a nonrotating configuration,  $M_{\text{TOV}} \simeq 1.2M_{\text{max}}$  [125]<sup>2</sup>. The merged object, instead, is in a metastable equilibrium supported by differential rotation, which has a quasi-universal rotation profile in case of quasi-circular merger remnants [58]. We evolve the simulations until the mass density flux at the detector placed at a distance of  $200 M_\odot \approx 300$  km becomes essentially zero. During this time, none of the merged objects has yet collapsed to a black hole.

## B. Mass ejection

We next discuss the properties of the ejected mass of all simulations shown in Table I. The amount of unbound mass

<sup>1</sup> Note that we here adopt the Newtonian definition of barycenter of a rest-mass density distribution.

<sup>2</sup> Given a law of differential rotation, a universal relation can be found also by the maximum mass supported through differential rotation and the maximum mass of a nonrotating configuration [126].

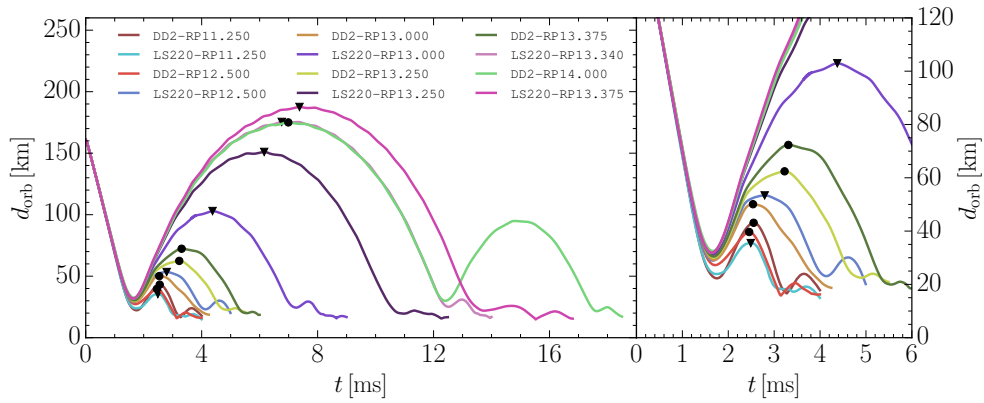


FIG. 2. Proper separation  $d_{\text{orb}}$  of the stellar barycenters for the equal-mass models as a function of time. The symbols mark the maximal separations after the first periastron passage. Note that the curves are truncated at the moment of merger.

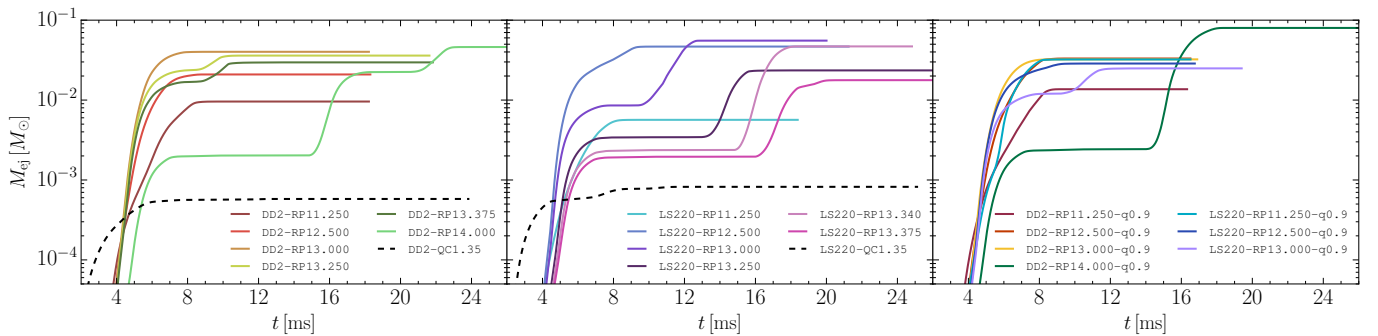


FIG. 3. *Left panel:* Dynamically ejected mass  $M_{\text{ej}}$  at a  $r = 200 M_{\odot}$  detector as a function of time for both EOS and the different periastron values listed in Table I. For comparison the same is shown for a quasi-circular binary of the same mass and EOS from [9]. Note that during a single periastron passage alone, more ejecta compared to an entire quasi-circular inspiral are produced. *Middle panel:* the same as the left panel but for the LS220 EOS. *Right panel:* the same as the left panel but for unequal-mass binaries with  $q = 0.9$ .

and its properties in terms of electron (proton) fraction, specific entropy and velocity are analysed as a function of the periastron separation  $r_p$  and the most important results are summarised in Table II.

As already discussed in Sec. II G 1, we analyze the ejected mass using a spherical detector at a coordinate radius of  $200 M_{\odot} \approx 300$  km. The total amount of unbound material is computed by integrating the rest-mass density flux of every fluid element on the sphere in time, as long as it obeys the geodesic criterion. The total amount of ejected mass is then given by integrating the mass flux over the whole sphere. Together with the mass flux we also compute the electron (proton) fraction, the specific entropy and the velocity of the unbound fluid elements.

We should note that we could have used detectors at larger distances than the reference one of  $200 M_{\odot} \approx 300$  km. While doing so would increase the amount of measured ejected mass (which can increase up to 30%), such measurement would also be quite inaccurate. This is because of two distinct reasons. First, as the ejected matter reaches more distant detectors its rest-mass density drops near the atmosphere level of the simulation, which, we recall, is already 11 orders of

magnitude smaller than the maximum rest-mass density in the simulations; in these regimes the numerical truncation error is clearly largest. Second, as the fluid expands and rarefies, the assumption of NSE used to construct the EOS tables is no longer correct, thus invalidating the analysis in these low-density regimes. In view of these considerations, we have preferred to use the measurements made on a detector which is not the largest one but provides us with more accurate results.

The dynamically ejected masses for the eccentric equal-mass binaries are shown in Fig. 3 for the two EOSs considered (see legend) and are compared with the corresponding ejected mass in the quasi-circular case for the DD2 EOS (dashed black line). It is quite clear that every single periastron passage in our models produces more ejecta than an entire quasi-circular merger, excluding longterm post-merger evolution. Overall, the models show very similar behaviour with cumulative outflows at every close encounter which last a few milliseconds. Note that shock-heating during merger essentially does not create additional amounts of unbound material or, if it does, this is overall negligible. Similar to the results in Refs. [59] for the LS220 EOS, the eccentric mergers considered in this work can lead to almost two orders of magnitude

Model	$M_{ej}$ [ $10^{-2} M_{\odot}$ ]	$\langle Y_e \rangle$	$\langle s \rangle$ [ $\frac{k_B}{\text{baryon}}$ ]	$\langle v_{ej} \rangle$ [c]	$J_{rad}$ [ $M_{\odot}^2$ ]	$E_{rad}$ [ $10^{-2} M_{\odot}$ ]
LS220-RP11.250	0.57	0.07	7.6	0.22	0.67	2.20
LS220-RP12.500	4.67	0.06	4.6	0.24	1.21	4.07
LS220-RP13.000	5.54	0.07	5.0	0.23	1.22	4.05
LS220-RP13.250	2.35	0.07	6.3	0.22	1.16	4.31
LS220-RP13.340	4.69	0.07	5.7	0.23	1.20	4.04
LS220-RP13.375	1.77	0.09	8.1	0.21	1.61	5.86
LS220-RP11.250-q09	3.22	0.04	2.3	0.22	0.65	2.13
LS220-RP12.500-q09	2.87	0.05	4.1	0.24	0.53	1.89
LS220-RP13.000-q09	2.49	0.07	6.0	0.23	0.94	3.27
DD2-RP11.250	0.96	0.12	8.9	0.23	0.93	2.94
DD2-RP12.500	2.09	0.05	4.4	0.23	0.78	2.42
DD2-RP13.000	4.02	0.05	3.2	0.26	0.75	2.60
DD2-RP13.250	3.60	0.06	4.9	0.25	0.80	2.39
DD2-RP13.375	2.96	0.06	5.2	0.24	0.76	2.37
DD2-RP14.000	4.61	0.10	7.2	0.21	1.04	3.21
DD2-RP11.250-q09	1.37	0.09	7.5	0.21	0.53	1.59
DD2-RP12.500-q09	3.31	0.05	4.2	0.22	0.41	1.20
DD2-RP13.000-q09	3.23	0.05	3.3	0.25	0.72	2.51
DD2-RP14.000-q09	7.99	0.06	2.8	0.22	0.45	1.33

TABLE II. Summary of the results for the eccentric binary systems under consideration. Listed are the dynamically ejected mass  $M_{ej}$ , the mass-averaged electron fraction  $Y_e$ , specific entropy  $s$  and ejecta velocity  $v_{ej}$  as well as the angular momentum  $J_{rad}$  and energy  $E_{rad}$  radiated by GWs.

larger ejected masses when compared to quasi-circular mergers (in this case we compare to models of [9] with the same mass and EOS).

The dependence of the ejected mass on the EOS, on the impact parameter and on the mass ratio of the binary can be appreciated from Fig. 4. First of all, the total amount of ejected mass is robust against the differences in the orbital parametrization, as well as the EOS and the mass ratio. Additionally, there is no definitive trend of larger mass ejection for unequal-mass binaries observed in quasi-circular binary neutron-star mergers, even though the lower mass companion is tidally disrupted at the second encounter. Note that for the unequal-mass models LS220-RP11.250-q09, DD2-RP11.250-q09, and DD2-RP12.500-q09, the ejected mass is larger than in corresponding equal-mass models. However, a further increase in  $r_p$  leads to the opposite behaviour, only DD2-RP14.000-q09 giving again a larger amount.

Note also that there are two local maxima in the ejected mass for the equal-mass models. The first one appears for  $r_p/R_1 \in [0.98, 1.02]$ , where  $R_1$  is the radius of the primary star in isolation; note that in such a range the stars merge after the second encounter. The second maximum is in a narrow range around  $r_p/R_1 \in [1.03, 1.07]$ , where the models undergo additional encounters, with the orbit getting more bound and less eccentric with each passage. In each of the three passages in models LS220-RP13.340 and LS220-RP14.000, the tidal interactions lead to subsequent large releases of unbound material. The additional encounter

in model LS220-RP13.340 is strongly suppressed due to the outer layers of both stars overlapping throughout the second encounter, leaving only the cores of both stars to separate slightly again before eventually merging.

Going beyond a periastron separation of  $r_p/R_1 = 1.07$ , as done for model LS220-RP13.375, the system merges again at the second encounter and thus produces less ejecta. Furthermore, when considering less eccentric orbits, multiple encounters do not only occur more easily, but are in fact unavoidable, see e.g., Refs. [50, 127]. For  $r_p/R_1 > 1.1$  we expect a recurrence of this pattern for fine-tuned initial orbital configurations, although exploring the space of parameters to this level of detail, possibly for critical behaviour, is beyond the scope of this paper.

In summary: the typical amount of ejected material is in the range of a few  $10^{-2} M_{\odot}$  up to almost  $10^{-1} M_{\odot}$ . As already conjectured in [59], the latter is expected to constitute an upper limit also for orbits undergoing more than two encounters. Since the system loses orbital energy and angular momentum with each close passage, the orbit becomes less eccentric and the amount of ejecta should approach that of quasi-circular binaries in the last few close passages. Moreover, we find that the models with multiple encounters lead to the largest amounts of unbound mass, thus providing a confirmation of the results found in [59, 128]. The largest amount of ejecta were produced by the DD2-RP14.000-q09 binary, which shows both a partial third encounter and tidal disruption of the lower mass companion.

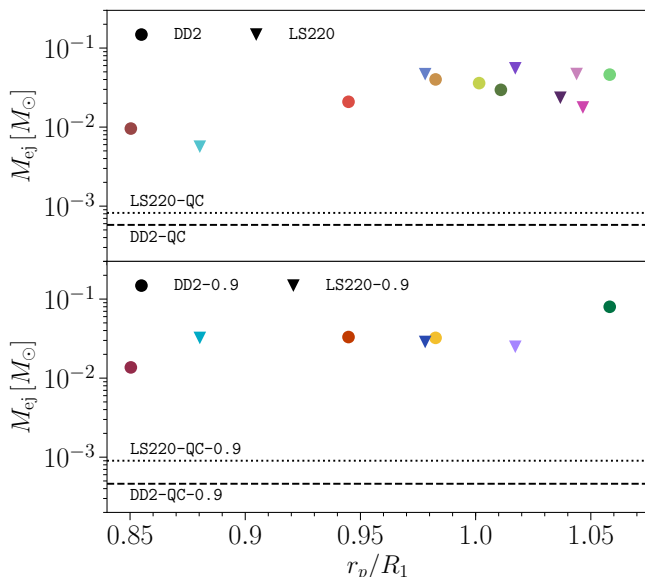


FIG. 4. Dynamically ejected mass  $M_{ej}$  at a  $r = 200 M_{\odot}$  detector as a function of the dimensionless quantity  $r_p/R_1$  for both EOS and mass ratios, where  $R_1$  is the TOV radius of the more massive companion. For comparison the same is shown for equal-mass quasi-circular binaries of the same mass and EOS from [9].

### C. Properties of the dynamical ejecta

In what follows we discuss the physical properties of the dynamical ejecta, namely: the average electron fraction  $Y_e$ , the specific entropy  $s$ , and the velocity  $v_{ej}$  of the ejecta; all of these properties are summarised in Table II for the binaries considered here.

A good general overview of the dynamics and properties of the (dynamical) ejecta is given in Fig. 5, which shows the equatorial  $[(x, y)$  plane] and meridional  $[(x, z)$  plane] slices through the simulation domain in terms of the electron fraction  $Y_e$  and temperature  $T$  (see colourcode). The latter is directly related to the entropy per baryon  $s$  and together with  $Y_e$ , they represent one of the most important quantities for the r-process nucleosynthesis taking place in the dynamical ejecta. More specifically, we show in the three columns of Fig. 5 the following binaries: a representative case of the DD2 EOS, DD2-RP13.375, which refers to a model with one periastron passage followed by the merger, the unequal-mass binary DD2-RP14.000-q09, which refers to the model with the largest amount of ejected material, and to the binary DD2-RP14.000, which represents a binary with three periastron passages and includes the merger. The three rows, instead, illustrate three different times throughout the simulation. The first shows the binary after the first periastron passage, the second row refers instead to a time after merger, and the third row shows when almost all the ejecta matter has crossed the  $200 M_{\odot}$  detector. Note, that for the DD2-RP14.000 binary the last passage before merger is the second, so we start from the second encounter.

In order to be efficient, the r-process requires a very neutron-rich environment from which neutrons can be accessed; hence, the electron fraction  $Y_e$  can be used to effectively describe the availability of such neutrons in the matter ejected during and after the merger. As described in Sec. II B, we model weak interactions by a leakage scheme, so that the electron fraction  $Y_e$  is not simply advected with the fluid, but can and does change due to electron and positron captures, in particular in the shock-heated material. In practice, a large value of the electron fraction is therefore a proxy for a relatively “neutron-poor” (electron rich) material, which will therefore lead to a suppressed r-process.

As can be inferred in Fig. 5, there is a clear difference in  $Y_e$  between the ejecta in the equatorial plane and the ejecta off the plane and, indeed, the distribution in  $Y_e$  can be associated to two different components. The first one comes from the cold neutron-rich material that is ejected by the tidal torques, while the second one originates from the shock-heated, high-temperature material. Both of these components can be recognised in Fig 5 as the equatorial and the polar components of the ejecta, respectively. Note, that due to both the higher electron fraction and the much lower density, the polar component of the ejected matter is a poor site for the r-process, in contrast to the matter ejected on the equatorial plane by tidal torques.

The distributions of  $Y_e$  in the dynamical ejecta for the equal-mass models are shown in Fig. 6, which also reports the corresponding distribution of a quasi-circular model of the same mass and EOS of [9] (dashed black lines). Note that the qualitative features of the distributions are very similar for the different models. This conclusion is slightly different from that reported in Ref. [59] and it is possible that the use of tracer particles can account for these small discrepancies.

An obviously prominent feature in the  $Y_e$  distributions in Fig. 6 are the peaks at very low values of the electron fraction, i.e.,  $Y_e \in [0.04, 0.08]$ , which are followed by a sharp drop to higher values of  $Y_e \lesssim 0.35$ . More importantly, the eccentric binaries are not able to reach the high  $Y_e$  tails that is instead achieved in the corresponding quasi-circular models. The only exception to this behaviour is given by the DD2-RP11.250 model, which shows a distribution much closer to the quasi-circular model, without showing the pronounced low  $Y_e$  peak of the other models. The reason behind this behaviour is that this model is undergoing a direct and violent merger without an additional periastron passage it is more similar to the quasi-circular case.

All in all, it is clear that the LS220 models are closer to the quasi-circular distribution, but with more material exhibiting lower  $Y_e$  values. Whether or not this can be explained purely by different stiffness, which would also be applicable to other EOS, cannot be answered with our limited data set, but appears reasonable on the basis of our simulations. For increasing periastron separation, the peak in the distributions is shifted to higher  $Y_e$  but stays well below 0.1. Comparing this behaviour to that of the DD2 models – with the exception of the special DD2-RP11.250 binary – this shift is absent and all models peak at  $Y_e \simeq 0.04$ . Leaving aside the differences across the various EOSs, it is apparent that neither the EOS nor the periastron distance have a significant impact on the  $Y_e$

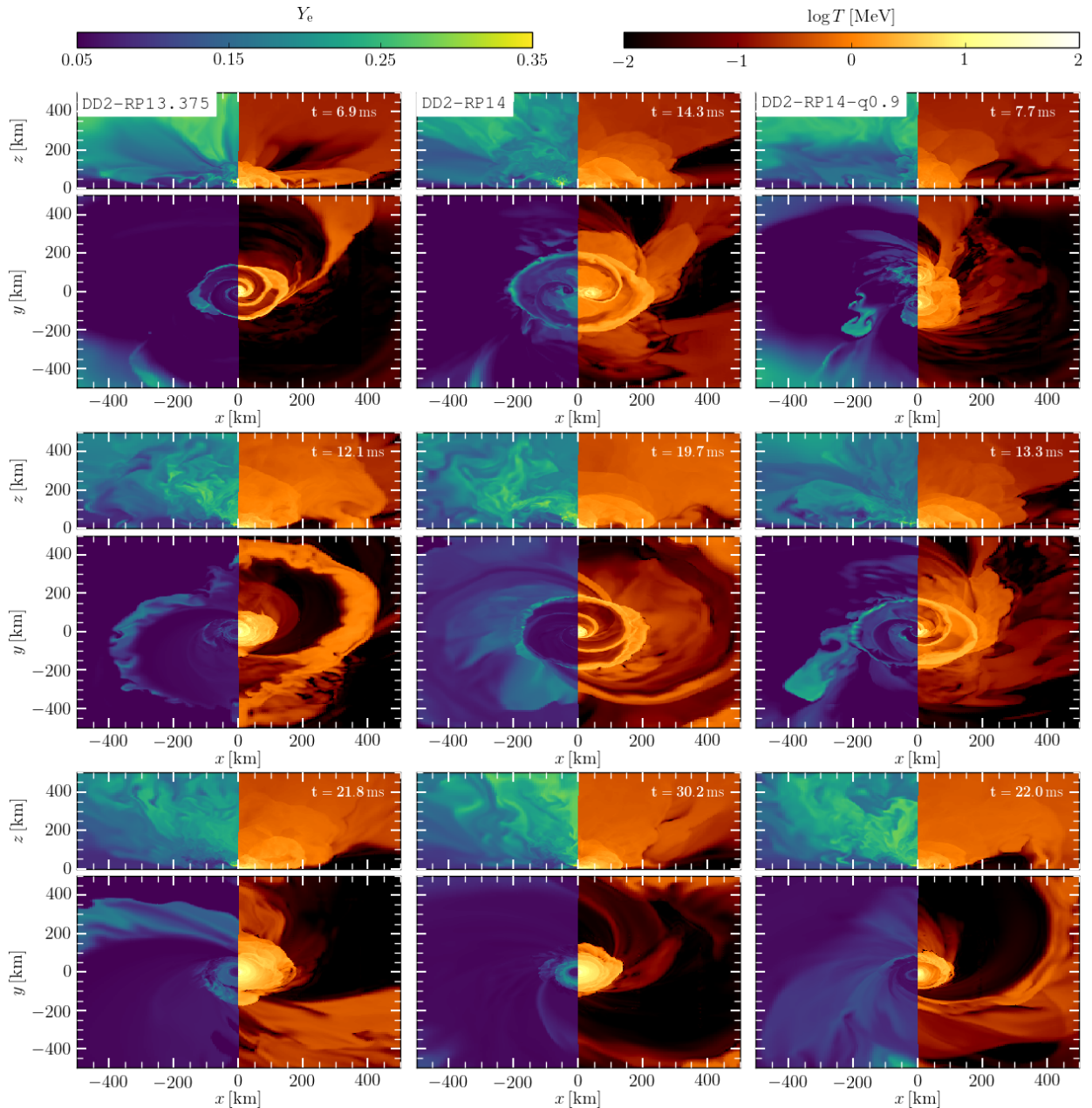


FIG. 5. Snapshots of the electron fraction  $Y_e$  and logarithmic temperature  $T$  in the equatorial ( $x, y$ ) and meridional ( $x, z$ ) plane for three models with DD2 EOS. Due to the different orbital dynamics different times are shown. For the DD2-RP13.375 and DD2-RP14.000-q0.9 models we show snapshots after the first encounter with the first ejecta (top) followed by the merger (middle) and ultimately the remnant when all ejecta crossed the  $200 M_\odot$  detector (bottom). The same is shown for DD2-RP14.000 but starting with the second encounter.

distribution, as long as the binary does not undergo a direct or almost head-on merger.

When considering instead the unequal-mass models, which are shown in the top-right panel of Fig. 6, the qualitative behaviour does not change considerably. The distributions feature again a peak at  $Y_e \lesssim 0.06$  and a sharp decline to higher values. The dynamical ejecta are dominated by extremely neutron-rich material, which is also clearly visible from the average  $Y_e$  of each model listed in Table II, where  $\langle Y_e \rangle \lesssim 0.1$

for all the models.

What is also clear from Fig. 6 is that – for a fixed EOS and mass ratio – there is a trend to produce distributions with systematically larger values of  $Y_e$  as the impact parameter is increased. This behaviour is not surprising as it is possible to consider the quasi-circular binaries (which reveal the largest electron-fractions) as a limiting case of eccentric binaries with very large impact parameter. Also, as can be seen from Fig. 3, the amount of ejected material is dominated by the second en-

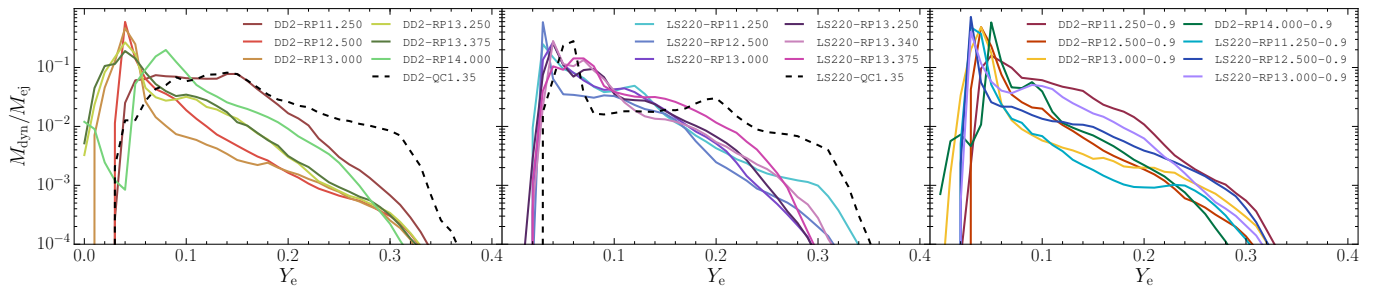


FIG. 6. *Left panel:*  $Y_e$  distribution of the dynamical ejecta masses  $M_{dyn}$  normalized to the total ejected mass  $M_{ej}$  at a  $r = 200 M_\odot$  detector for the equal-mass binaries listed in Table I. For comparison the same is shown for a quasi-circular binary of the same mass and EOS from [9]. *Middle panel:* the same as in the left panel but for the LS220 EOS. *Right panel:* the same as in the left panel but for the  $q = 0.9$  binaries listed in Table I.

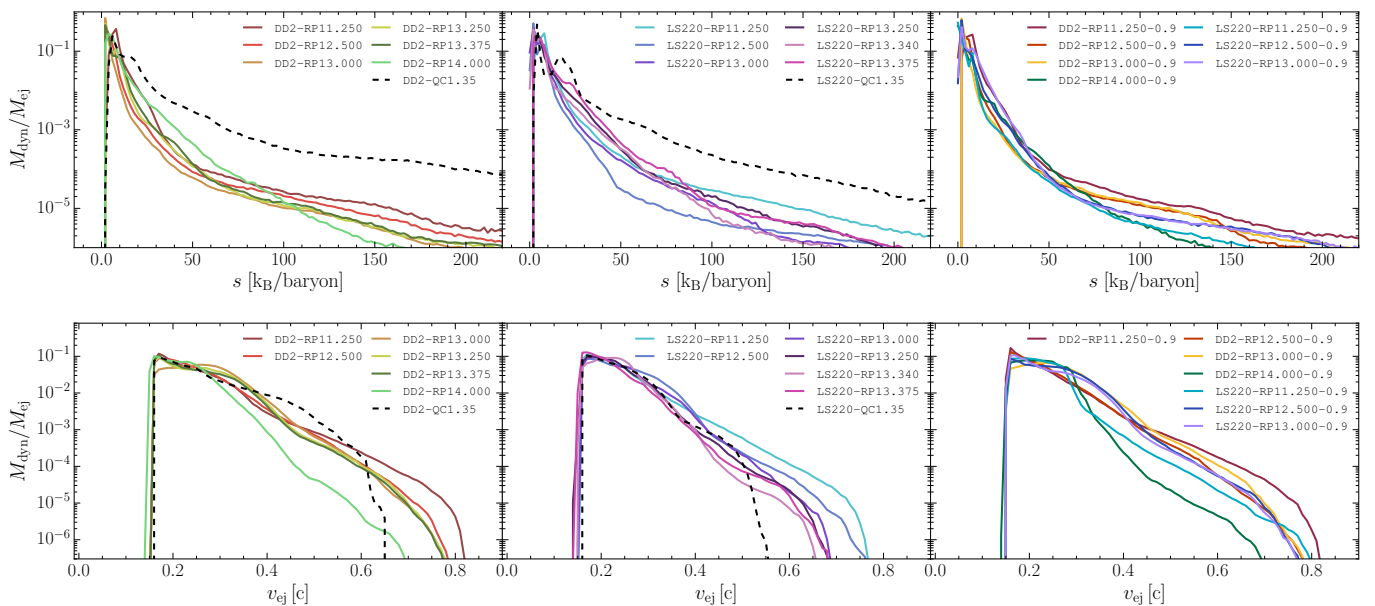


FIG. 7. The same as in Fig. 6, but for the distribution of the specific entropy (top panels) and for the distribution of the velocity of the ejected material (bottom panels).

counter for the models with  $r_p/R_1 \gtrsim 1.03$ , so that the binary has already lost a large part of its initial eccentricity and the orbit is thus much closer to a quasi-circular one.

The considerations made above, while robust, neglect what could be an important effect on the  $Y_e$  distribution, namely, the accounting for neutrino absorption in the ejecta. This process, which can be modeled by a more sophisticated radiative-transfer scheme (e.g., an M1-scheme) has been shown that when taken into account in simulations of compact binaries in quasi-circular orbits, e.g., in Refs. [129–133], can lead to overall higher values of  $Y_e$ . We leave the investigation of the impact of neutrino absorption on eccentric binary merger ejecta to future studies.

The second important thermodynamic quantity for the r-process is the entropy per baryon, whose distribution is shown in the top panels of Fig. 7. This quantity is intimately connected to the shock-heated matter in the ejecta, so that the ma-

terial of higher temperature visible in Fig. 5 effectively trace material with larger entropy. In turn, the entropy produced in these shocks impacts the neutron-to-seed ratio of the material and has therefore a direct influence on the r-process and the nucleosynthesis. As can be seen in Fig. 5, most of the equatorial ejecta are of low temperature when compared to the low-density outflow in the polar region, as well as to the shock-heated remnant. Hence, most of the matter is expected to have rather low values of the entropy, as shown by the entropy distributions in the top panels of Fig. 7, which have a pronounced peak at very low values, i.e.,  $s \lesssim 10 k_B/\text{baryon}$ , and exhibit a sharp decline for larger values. Note also that the tail to higher entropies that is present in the quasi-circular models, is completely absent for both EOS. This is again because most of the matter ejected in these eccentric binaries is at low temperature.

As for Fig. 6, also the top-right panel of Fig. 7 reports

the entropy distributions in the case of unequal-mass binaries. Note that there does not appear to be any systematic trend towards the distributions measured with quasi-circular binaries, which is suggestive of the fact that shock heating in the ejecta is strongly suppressed.

As mentioned above, Table II reports, among other quantities, also the average (median) values of the electron fraction and of the entropy  $\langle Y_e \rangle$  and  $\langle s \rangle$ . An investigation of the results in the table reveals that the dynamical ejecta are dominated by cold and neutron-rich matter, which is ejected during the close passages at periastron by tidal torques. Any further ejection by shock-heating is negligible, as long as one excludes those mergers that occur with very small impact parameter and hence represent essential “head-on” collisions. These conclusions are robust against variations in the EOS, the periastron parametrization and the mass ratio of the system.

Finally, we show in the bottom panels of Fig. 7 the distributions of the velocities of the ejecta (see also Table II for the average values), which is the third key property of the ejected material and plays an especially important role in calculations of lightcurves from kilonova emission. Note that in a way similar to the distributions of quasi-circular binaries, the ejecta exhibit velocities of at least 0.15 and strongly peaks after that, leading to average velocities of 0.21 – 0.25 and a long tail of velocities of up to 0.8. Note also that because smaller impact parameters lead to larger shocks and hence to larger accelerations, the distributions show an increase in the slow component and a decrease in the fast component of the ejecta as the impact parameter is increased. Indeed, the loss of a high-velocity tail is particularly evident in the case of the DD2 binaries. Finally, this overall behaviour does not change considerably when considering unequal-mass binaries, as shown in the bottom-right panel of Fig. 7.

#### D. r-process nucleosynthesis

As mentioned in the Introduction, the study of the ejected matter is particularly important because of its nuclear evolution once it has left the system and undergoes nucleosynthetic reactions via the r-process. In our approach, the r-process yields are computed using the setup of tracer trajectories described in Ref. II G 2 and in which a subset of the complete set of tracers is selected following the prescription described in [9] to avoid the need of running the nuclear network for every single tracer trajectory and to define an unambiguous mass weight for each of them. In practice, our use of tracers and their input in the nucleosynthetic analysis can be summarised as follows. First, the unbound tracers are collected from all tracers of a simulation based on the geodesic criterion. Second, instead of selecting a subset randomly from the unbound tracers, we randomly select a representative tracer for a specific value of the electron fraction and of the specific entropy. To accomplish this we take the  $Y_e$  and specific-entropy distributions of the ejecta at the  $200 M_\odot$  detector and bin them into a two-dimensional histogram. Using then the knowledge of these two quantities for every tracer at the moment it passes the detector, it is possible to sample one tracer for each bin.

The mass weight of each tracer is naturally the mass fraction of the bin it was sampled from. This prescription ensures that the whole range of possible combinations are properly covered and weighted accordingly. Using this procedure, each model effectively leads to  $\sim 2000$  tracer trajectories that are then trimmed and extended as described in Sec. II G 2.

Furthermore, since we wish to carry out a comparison with the nucleosynthetic yields and r-process abundances from quasi-circular orbits computed in Ref. [9], and since the latter employed a different nuclear-reaction network code, we apply the same procedure described above also to tracers computed from quasi-circular binaries. In other words, instead of comparing the abundance curves computed here with those reported in [9], the r-process abundances from quasi-circular binaries are recomputed with the same setup employed in this paper. In this manner, we eliminate any possible bias effect related to differences in the nuclear rates or nuclear-reaction network codes and can thus perform a meaningful comparison.

The final abundance patterns of the r-process of all models considered in this work and as computed with the nuclear-reaction network code `SKYNET` are shown in Fig. 8 as a function of the atomic mass number  $A$ . These abundances are supplemented by the recomputed quasi-circular (dotted black lines) and solar r-process abundances (black solid circle). All curves are normalized to unity in the given mass number interval to eliminate the need of choosing a special but arbitrary element to normalise to. The top panels refer to binaries with equal masses (one for each of the two EOSs considered), while the bottom panels show the results for unequal-mass binaries, again for the two EOSs. In all cases, the different lines refer to different values of the initial periastron parametrization.

Overall, the results reported in Fig. 8 clearly show that all models considered in this work are able to reproduce the general behaviour of the solar r-process element abundances, starting from the second r-process peak at  $A \simeq 130$  and up to the third peak at  $A \simeq 195$ , including the rare-earth elements in between. Furthermore, while differences in the properties of the ejecta from quasi-circular and eccentric binaries have been discussed in Sec. III C, these do not really impact the final abundances, which are found to reproduce equally well Solar abundances for both classes of binaries. In summary, these results confirm the findings of previous works and confirm that the merger of binary systems of neutron stars can reproduce robustly, i.e., in a way that is insensitive to the details of the EOS, mass ratio, and orbital dynamics, the Solar abundances of heavy r-process elements.

#### E. Gravitational-wave emission

The gravitational waveforms computed from our eccentric binaries and reported<sup>3</sup> in Figs. 9–11, follow the same over-

<sup>3</sup> Note that the duration of the waveforms in Figs. 9–11 is different for different binaries as the simulations for binaries with multiple encounters ob-

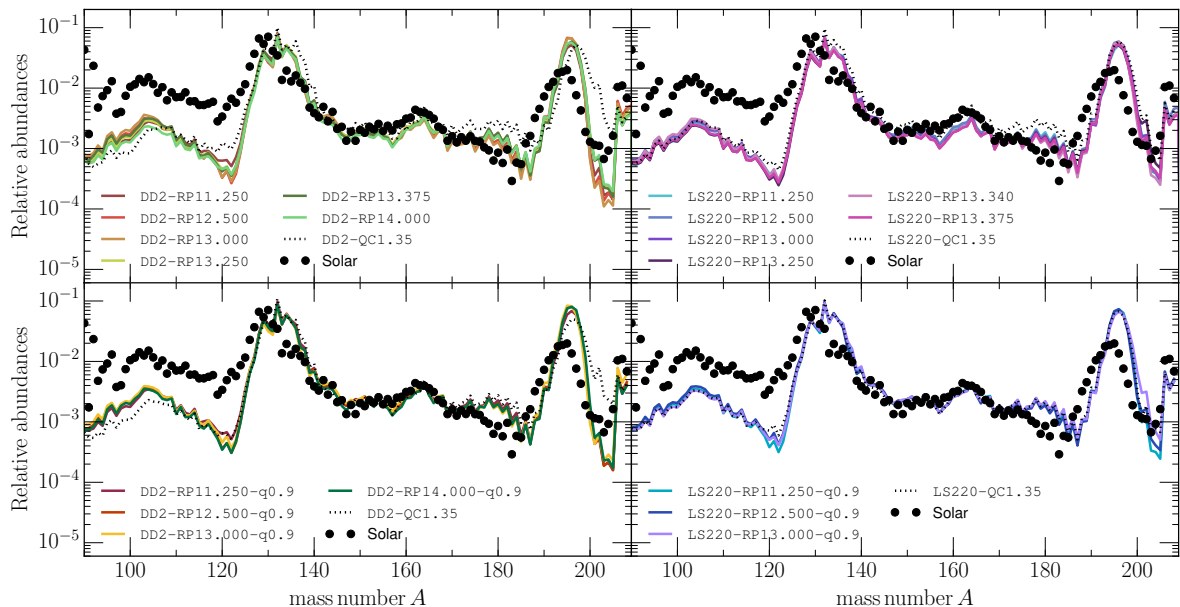


FIG. 8. Final abundances of the  $r$ -process yields from a representative subset of unbound tracer trajectories for the equal-mass and  $q = 0.9$  binaries listed in Table I together with the solar abundances shown as black circles. We also show the abundances resulting from the tracers of the quasi-circular mergers of the same mass and EOS from [9].

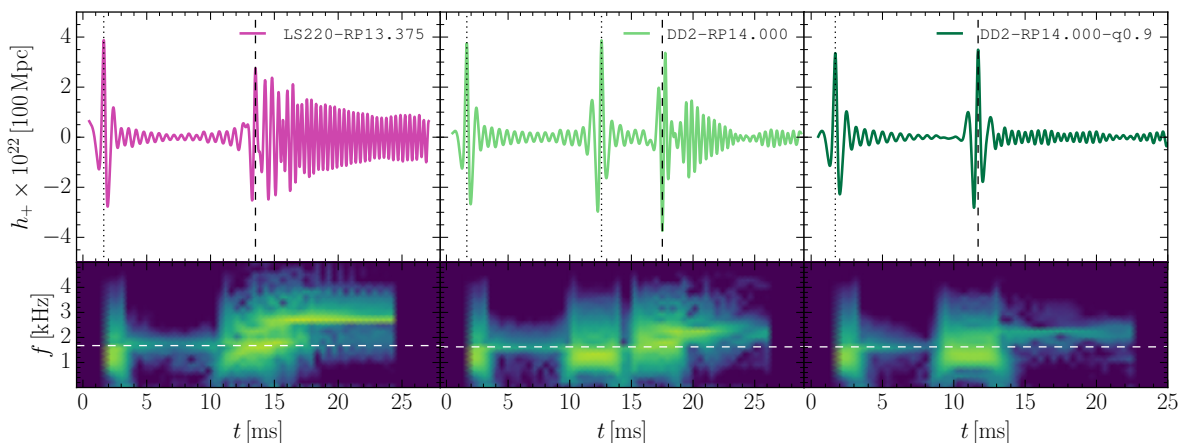


FIG. 9. Gravitational-wave strain of the  $\ell = m = 2$  mode for a source at 100 Mpc distance and its spectrograms for different  $r_p$ , EOS and  $q$ . Shown with a white dashed line are the respective  $f$ -mode frequencies while the time of periastron approach is marked with a vertical dotted and the time of merger with a vertical dashed black line. Note that there is significant power from the  $f$ -mode after the pericenter burst, which is well separated in time, from the contributions at similar frequencies during merger.

all behaviour observed in previous investigations of [50, 134]. More specifically, at close passages the orbital dynamics of the binary gives rise to the GW bursts that are typical of highly eccentric binaries. Such bursts are then separated in time by the GWs associated with those oscillations that have been excited at the close-periastron passage and that reflect the response of the stars to the fundamental mode of oscillation, or

$f$ -mode. This is shown in particular in Fig. 9, which reports in the top panels the gravitational waveforms for the set of three binaries at a distance of 100 Mpc with particular long waveforms, while it offers a view of the corresponding spectrogram<sup>4</sup> in the lower panels. Indicated with a horizontal dashed white line is the frequency of the  $f$ -mode oscillation of each indi-

viously require longer integration times.

<sup>4</sup> To produce the spectrogram we apply a Tukey window with a shape parameter of 0.25, a window length of 4.5 ms and an overlap of 4.0 ms.

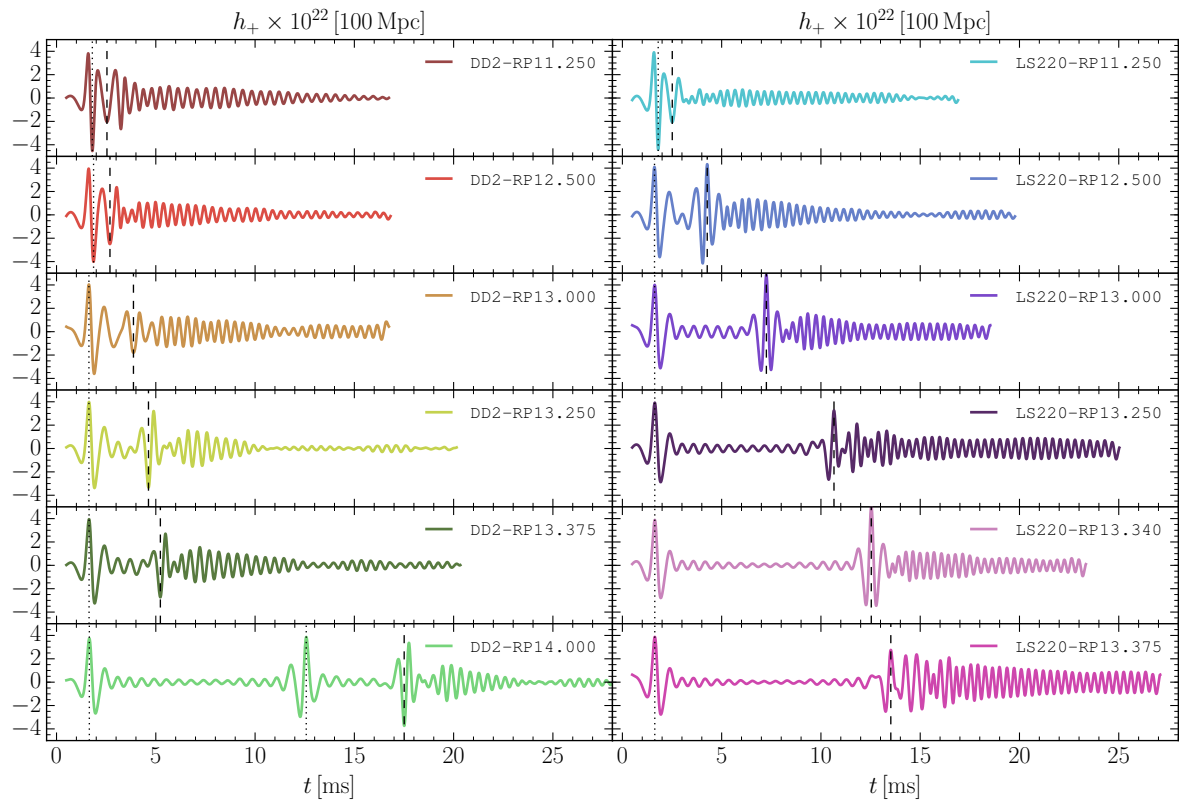


FIG. 10. Gravitational-wave strain for a source at 100 Mpc distance. The time of periastron approach is marked with a vertical dotted and the time of merger with a vertical dashed black line.

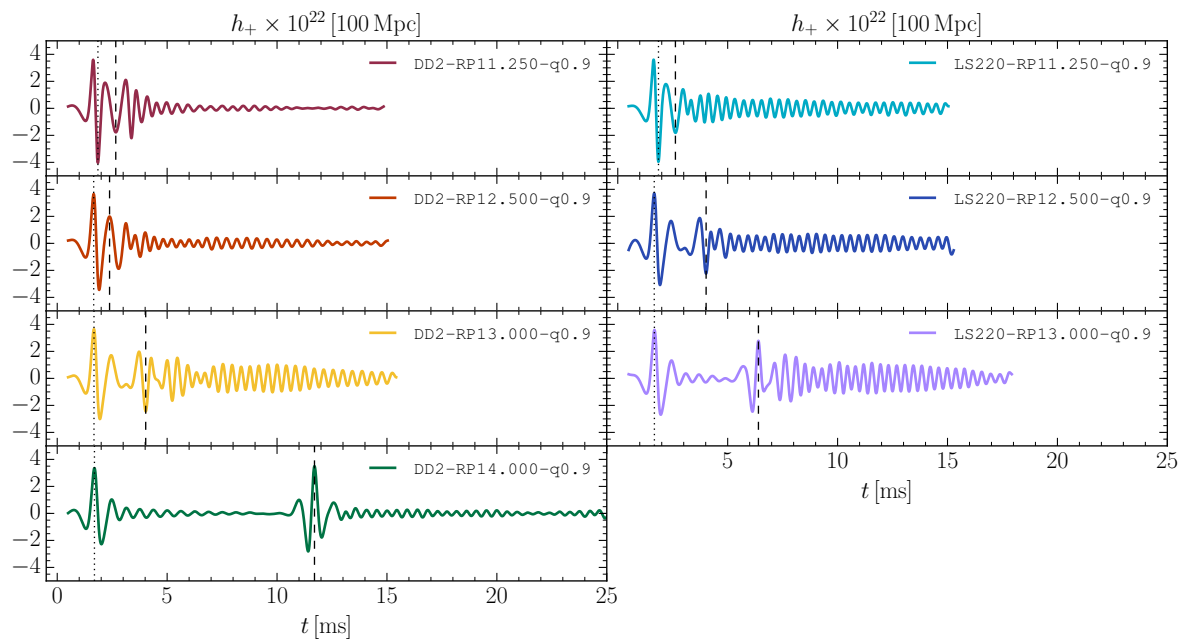


FIG. 11. The same as in Fig. 10 but for the unequal-mass binaries.

vidual neutron star model in isolation that is triggered after the first encounter (before merger) and similarly for the main  $f_2$  peak frequency of the hypermassive neutron star during the post-merger signal (see [45, 46, 48] for a classification of the spectral features of the post-merger signal). The spectrograms reveal more clearly what can already be seen from the waveforms, namely, that a substantial portion of the energy in the signal lies in narrow frequency bands corresponding to the  $f$ -modes of oscillation of the individual stars, which are then followed by the oscillations of the HMNSs after the merger. Since these  $f$ -mode oscillations depend on the internal structure of the stars, their measurement would yield an independent avenue to constrain the neutron-star mass in addition to the information from the inspiral and/or post-merger waveform thereby breaking parameter degeneracies and allowing a more accurate determination of source parameters if accurate templates are available.

Since their damping is mostly due to the GW emission, these oscillations can be long-lived, so that at the onset of merger the waveforms may still exhibit features due to eccentricity depending on details of the orbit [50, 127]. When considering the various binaries reported in Fig. 9 (which refers to equal-mass binaries) and focusing on the periastron approach (which is marked with a vertical dotted black line) and to the time of merger (which is marked with a vertical dashed black line), it is easy to appreciate that as the impact parameter is increased from top to bottom, the binaries experience either a single periastron approach (top panels), two periastron approaches (middle panels), or even three periastron approaches (bottom-left panel).

Note also that when keeping fixed the EOS and the impact parameter  $r_p$ , the strongest tidal interactions occur in the equal-mass systems. This can be most easily deduced when comparing the middle and right panels of Fig. 9, which report the DD2 binaries with  $r_p = 14 M_\odot$  and mass ratios  $q = 1$  and  $q = 0.9$ , respectively. In particular, it is easy to see that the  $f$ -mode oscillations triggered after the first encounter are larger and longer-lived in the equal-mass case. This is because although the tidal torques are not necessarily the largest<sup>5</sup>, in the equal-mass case the two excited stars resonate at exactly the same frequency and hence produce a stronger GW signal (middle panel). By contrast, in the unequal-mass case (right panel), the two stars oscillate at slightly different frequencies and the corresponding GW signal is rapidly suppressed.

For the models shown in Figs. 9–11 – whose first periastron encounter is again marked with a vertical dotted black line, while merger with a dashed black line – the post-merger waveforms exhibit the well-known features associated with an HMNS, with spectral features that show clear peaks [43–47, 135], following universal relations [46, 48]. Furthermore, it is clear from Figs. 9–11 that the LS220 EOS, being slightly stiffer than the DD2 EOS, typically yields – all else being

equal – a stronger GW emission during the HMNS phase (see also Ref. [48] for a detailed discussion). At the same time, it should be noted that given the typical masses and radii of neutron stars, and the fact that the fundamental mode frequency scales like the average rest-mass density, i.e.,  $f \simeq (M/R^3)^{1/2} \gtrsim 1$  kHz, these frequencies generically fall in a range where the advanced GW detectors [adLIGO and advanced Virgo, (ad)VIRGO]] have lower sensitivity as they are limited by the laser shot-noise. Hence, future third-generation detectors, such as ET or CE, or any detector with recently suggested upgrades [33, 34], are certainly better suited for the detection of the GW signal from eccentric binaries.

The first detections of such rather rare systems are expected to come from sources at larger cosmological distances [136]. For quasi-circular binaries, the properties of the GW emission lead to huge detector volumes out to  $z \leq 3$  (ET) and  $z \leq 6$  (CE), also because the GW signal is shifted to frequencies where the detectors are more sensitive. Detection efforts of gravitational waves from eccentric binaries will also benefit from the cosmological redshift of the frequency of either the  $f$ -mode oscillations or that of the post-merger signal with intrinsic frequencies of a few kHz in the source frame. Due mostly to the lack of substantial power at lower frequencies, the sources studied here can be seen out to more modest, but still large distances of about  $z \gtrsim 0.5$ .

To illustrate this effect, we compare in Fig. 12 the PSDs from some of our models to the noise equivalent strain due to the detector noise for adLIGO, ET and CE at design sensitivity considering a source distance of  $\sim 100$  Mpc), i.e.,  $z = 0.023$ , marking the different binaries with the same colorcode used in the previous figures 9–11. Also shown as a comparison is the corresponding signal for a binary in quasi-circular orbit and with the LS220 EOS. Note that for the eccentric cases a good portion of the power is located in a somewhat broad bump around 1 kHz with a high-frequency modulation that is most likely due to the short duration of the signals and to the bursts at the periastron and then at the merger (see Appendix A for a discussion with a toy model). Also clearly shown in the PSDs are the peaks associated with the  $f$ -mode oscillations, as well as the  $f_2$  peaks of the post-merger signal<sup>6</sup>.

When comparing the PSDs from eccentric and quasi-circular binaries it is apparent that the latter benefit from a considerable amount of power accumulated during the inspiral, which is much reduced in the case of eccentric mergers and, more importantly, does not follow a simple  $f^{-7/6}$  behaviour with frequency and that makes it amenable to searches with GW templates. Indeed, bursts-type searches based on unmodeled features and an extensive use of spectrograms such as those shown in Fig. 9, are possibly the most effective way of searching for this type of signals. Overall, the lack of this low-frequency portion reduces the overall SNR and implies that dynamical-capture signals will be in general harder to

<sup>5</sup> For extended objects such as neutron stars, the torque will depend sensitively on the mass, the mass-radius relation and the orbital frequency, all of which depend themselves on the EOS. It is therefore possible that the maximum torque is not attained in the case of equal-mass binaries.

<sup>6</sup> The emission from the HMNS oscillations was followed only for the timescale of the simulations but could actually be much more long-lived, increase the signal power at least as the square root of the emission time.

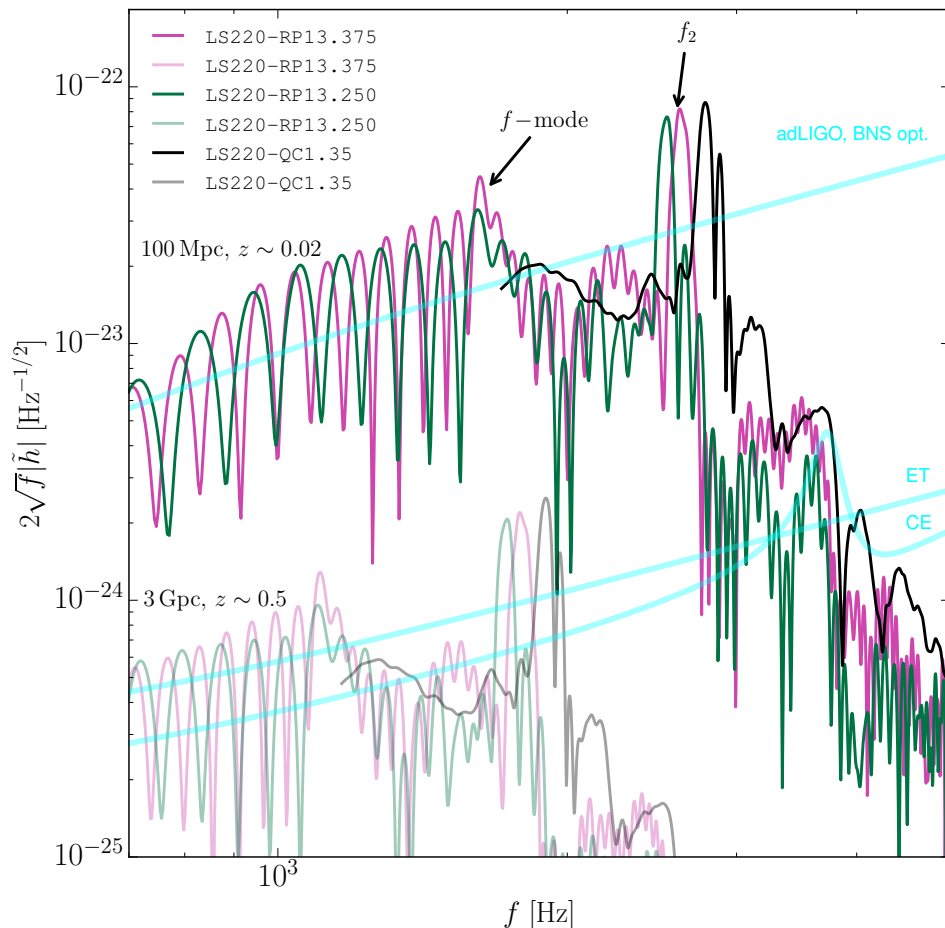


FIG. 12. PSDs from some of our binaries at a distance of  $\sim 100$  Mpc, i.e.,  $z = 0.023$ , reported with the same colorcode used in Figs. 9–11, together with the detector sensitivities for adLIGO, ET and CE at design sensitivity. Also shown as a comparison is the corresponding signal for a binary in quasi-circular orbit and with the LS220 EOS. Note that a good portion of the power is located in a somewhat broad bump around 1 kHz with a high-frequency modulation due to the short duration of the signals and to the bursts at the periastron and then at the merger. Note also the peaks associated with the  $f$ -mode oscillations, as well as the  $f_2$  peaks of the post-merger signal. Finally, reported with the same colours but semitransparent lines, are the same PSDs when the sources are taken to be at a larger distance of 3 Gpc, i.e.,  $z = 0.5$ .

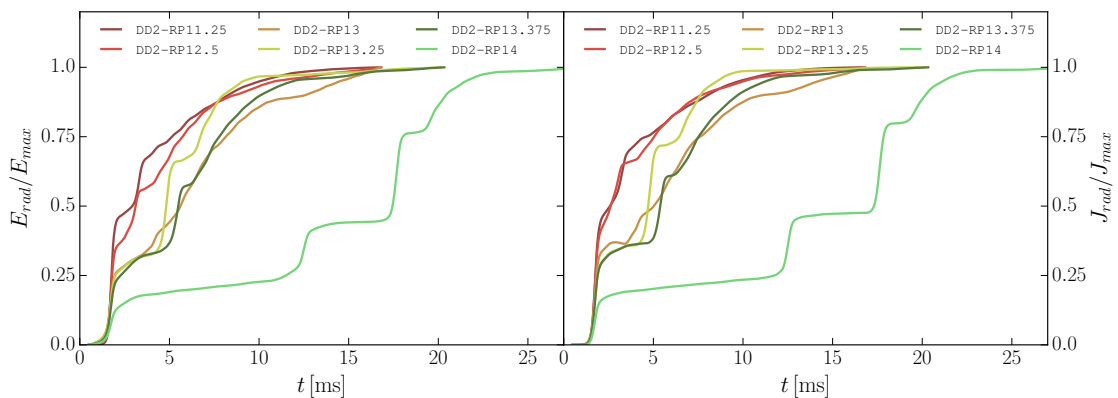


FIG. 13. Energy  $E_{rad}$  and angular momentum  $J_{rad}$  with respect to the total energy  $E_{max}$  and total angular momentum  $J_{max}$  radiated by GWs as a function of time for different values of  $r_p$  for the DD2 EOS.

detect than quasi-circular binaries with the assumed detector characteristics (all else being equal).

Also shown in Fig. 12 with the same colours but semitransparent lines, are the same PSDs when the sources are taken to be at a larger luminosity distance of about 3 Gpc, corresponding to redshift of  $z = 0.5$ . The gravitational redshift of which the signal will be subject to in this case, and the corresponding decrease in power due to the larger distances, will obviously make it undetectable by adLIGO, but still within the detection horizon of third-generation detectors such as ET or CE, despite the smaller power at low-frequencies contributing to the SNR.

In summary, despite the difficulties of detecting the GW signal from such systems, the combined benefits of having a very large detection volume (which counters the low event rate) and the shift to lower frequencies of the bulk of the emission (which counters the low sensitivity of the detectors), considerably increases the chances of detecting the GW emission from eccentric binaries by third-generation detectors.

Finally, we show in Fig. 13 the energy,  $E_{rad}$ , and angular momentum,  $J_{rad}$ , radiated by GWs as a function of time for different values of the initial impact parameter and for the equal-mass binaries with the DD2 EOS. As can be appreciated from the two panels, the efficiency in the emission of GWs is very large around the time of closest approach, when the actual luminosity reaches values of  $\simeq 5 \times 10^{55}$  erg/s, and where large fractions (up to 50%) of the total radiated energy and angular momentum are emitted. Note also that the GW waveforms associated with these bursts can be easily modeled by sine-Gaussian and hence their presence in the detector's signal can easily and efficiently be matched-filtered to be revealed. Furthermore, it is important to note that for a given EOS the total radiated energy does not have a simple monotonic behaviour with the initial impact parameter. More specifically, while the brightness of the GW burst decreases with  $r_p$  for binaries having only one encounter – so that, for instance, the binary DD2-RP11.250 radiates more than DD2-RP13.375 – the total radiated energy increases with the number of encounters, so that at the end the binary DD2-RP14.000 is actually more luminous than DD2-RP11.250. Finally, note that the time intervals between two encounters, when the  $f$ -mode oscillations are excited, the GW emission is steady and the radiated energy and angular momentum are simple and almost linear functions of time.

#### IV. CONCLUSIONS

We have presented the most extensive investigation to date of eccentric binary neutron-star mergers in full general relativity and encompassing 19 different configurations. In this way, we were able to explore the impact of various degrees of freedom of the system – the orbital eccentricity (or impact parameter), the EOS and the mass ratio – on the bi-products of the merger, namely, the GW emission, the dynamically ejected matter, and the nucleosynthetic yields.

Our numerical approach is based on the CCZ4 formulation of the Einstein equations, whose constraint-damping capabil-

ities make it particularly suited to study a system involving initial data with considerable violation of the constraints. For the dynamically ejected mass, on the other hand, we employ a standard criterion for unbound material and track it via tracer particles that are passively advected with the fluid flow. We use a novel approach to seeding the tracer particles both at the first periastron and first apoastron respectively to better capture the peculiarities of eccentric binaries, while minimising potential tracer-selection bias. These resulting diagnostic quantities from these tracers are then interfaced with the separate SkyNet nuclear-reaction network code that produces nucleosynthetic yields.

Overall, our results indicate that eccentric binary neutron-star mergers universally produce considerably more ejected mass, i.e.,  $10^{-2} - 10^{-1} M_{\odot}$ . Furthermore, these ejecta are faster (with long tails of the distribution up to 0.8) and with a composition that depends on the EOS, but is distinct from that of merging systems on quasi-circular orbits. Also quite generically, we can identify a component of the dynamically ejected material that is lost near the equatorial plane and that is characterised by much lower temperatures and low  $Y_e$  as a result of the very small shock heating experienced by this matter. On the other hand, matter ejected around the polar regions does not appear to be a promising site for r-process nucleosynthesis due to its relatively high values of  $Y_e$ , high temperatures and low densities.

Despite some of these striking differences between eccentric and quasi-circular binaries, the final nucleosynthetic yields do not depend on the EOS and reproduce the main features of the observed relative abundances and, in particular, the second and third peak of the heavy-elements distribution. This is a particularly important result: since a similarly good match with the observations has been obtained by several authors when considering quasi-circular binaries, it is quite apparent that the merger of binary neutron stars leads to a nucleosynthesis that reproduces the observed abundances with little dependence on the orbital dynamics, on the EOS, the total mass and the mass ratio.

Finally, we have computed the GW emission focusing on  $f$ -mode oscillations before and after merger finding that the imprints of  $f$ -mode oscillations in the GW signals depend most strongly on the orbital configuration and mass ratio of the binary, but are rather uniform across different EOSs. We attribute differences to the appearance of  $f$ -mode features in GWs to the different tidal interactions both in terms of excitation and response. In our analysis we also include the cosmological redshift of the GW signal from large distances, and illustrate how this brings the signal into a more sensitive regime of third-generation detectors. We also show that, while some of the systems under investigation can be very challenging to detect even for the ET or CE, other configurations with longer signals, more cycles and low-frequency contributions are detectable out to distances as large as  $z \gtrsim 0.5$ , despite the lack of low-frequency cycles that are such an important contribution in quasi-circular signals. Detector sensitivity at high frequencies around 1 kHz are key to detecting such sources.

Various effects have not been taken into account in this work, such as magnetic- and neutrino-driven winds, viscous

heating in the surrounding tori and magnetic fields, which operate on longer timescales can increase the ejected mass [137–146]. In particular, it has been shown in Ref. [59] that neglecting neutrino cooling can lead to an overestimation of the ejected mass. Another important process could be neutrino heating modeled by an M1-scheme [131, 133]. This could lead to even more unbound material as has been shown in [129]. All of these aspects of the dynamics of merging eccentric binaries will find improvement in future work.

### ACKNOWLEDGEMENTS

It is a pleasure to thank Luke Bovard, Jonas Lipuner, Moritz Reichert, Marius Eichler, Elias Most, Charles Horowitz, Huan Yang, and Eric Poisson for numerous discussions and useful input. Support comes also in part from “NewCompStar” and “PHAROS”, COST Actions MP1304 and CA16214; LOEWE-Program in HIC for FAIR; European Union’s Horizon 2020 Research and Innovation Programme (Grant 671698) (call FETHPC-1-2014, project ExaHyPE), the ERC Synergy Grant “BlackHoleCam: Imaging the Event Horizon of Black Holes” (Grant No. 610058). The simulations were performed on the SuperMUC cluster at the LRZ in Garching, on the LOEWE cluster in CSC in Frankfurt, on the HazelHen cluster at the HLRS in Stuttgart.

### Appendix A: On the appearance of multiple bursts containing similar frequencies in GW spectra

In this Appendix we illustrate through several simple analytical toy models that mimic the basic features in our waveforms, how GWs with more than one burst can lead to non-continuous PSDs. We build the toy model combining various contributions from the following elements, that are representative of features we observe in our gravitational waveforms. In particular, given a kernel

$$b(t, t_{burst}, \sigma, \omega) := \exp[-(t - t_{burst})^2/\sigma] \sin(\omega t), \quad (\text{A1})$$

the signals are then explicitly formed as

$$s_1 := b(10^3, 10^5, 1/20) + (1/10) \sin(t/100) + b(4 \times 10^3, 8 \times 10^4, 1/22), \quad (\text{A2})$$

$$s_2 := b(10^3, 10^5, 1/20) + (1/10) \sin(t/50), \quad (\text{A3})$$

$$s_3 := e^{-(t-10^3)^2/5 \times 10^4} + e^{-(t-3 \times 10^3)^2/5 \times 10^4}. \quad (\text{A4})$$

where  $t$  is uniformly spaced on the interval  $[0, 5000]$  using  $10^4$  points.

Equation (A2) constitutes a model with two bursts, as well as a sinusoidal wave analogous to the  $f$ -mode signal. This signal, termed “2 bursts +  $\sin(\omega t)$ ” in Fig. 14, exhibits a non-continuous structure where regions of high power are separated by small (in frequency) regions with very low power. This behaviour is very similar to our eccentric GW PSDs in Fig. 9, despite the fact that our toy models are fully analytic and smooth functions of time. This implies that the non-continuous structure shown in Fig. 9 is not an artefact due to the poor sampling of the GWs. Interestingly, also other toy models show the same behavior as long as there are two bursts that can interfere with each other. In contrast, models with only one burst (even with an additional periodic component) are more akin to quasi-circular waveforms do not show such non-continuous PSDs.

To further confirm this interpretation we have computed GW spectra from a subset of the GW signals and consistently found that whenever we filter out all bursts except for one (either the one at periastron or at merger) the non-continuous structure disappears, as expected based on the analysis summarised above.

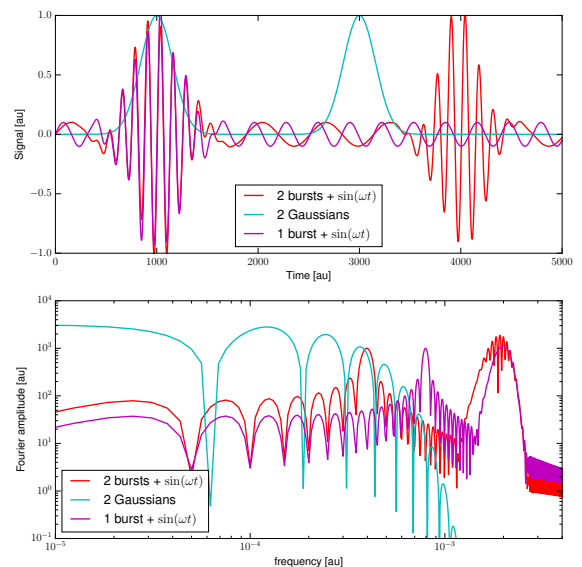


FIG. 14. Three toy-model signals illustrating well-known relations between the time domain and frequency domain: A sinusoidal signal with one (magenta) or two (red) bursts and a signal composed of two pure Gaussians with no periodic component (cyan). All signals are zero-padded such that their length increases by a factor of 8.

[1] The LIGO Scientific Collaboration and The Virgo Collaboration (LIGO Scientific Collaboration and Virgo Collaboration), *Phys. Rev. Lett.* **119**, 161101 (2017)

[2] The LIGO Scientific Collaboration, the Virgo Collaboration, B. P. Abbott, R. Abbott, T. D. Abbott, F. Acernese, K. Ackley, C. Adams, T. Adams, P. Addesso, and et al. (LIGO Sci-

- entific Collaboration and Virgo Collaboration), *Astrophys. J. Lett.* **848**, L12 (2017)
- [3] R. Narayan, B. Paczynski, and T. Piran, *Astrophys. J. Lett.* **395**, L83 (1992), [astro-ph/9204001](#)
- [4] D. Eichler, M. Livio, T. Piran, and D. N. Schramm, *Nature* **340**, 126 (1989)
- [5] L. Rezzolla, B. Giacomazzo, L. Baiotti, J. Granot, C. Kouveliotou, and M. A. Aloy, *Astrophys. J. Letters* **732**, L6 (2011), [arXiv:1101.4298 \[astro-ph.HE\]](#)
- [6] V. Paschalidis, *Classical and Quantum Gravity* **34**, 084002 (2017), [arXiv:1611.01519 \[astro-ph.HE\]](#)
- [7] B. D. Metzger, *Living Reviews in Relativity* **20**, 3 (2017), [arXiv:1610.09381 \[astro-ph.HE\]](#)
- [8] L. Baiotti and L. Rezzolla, *Rept. Prog. Phys.* **80**, 096901 (2017), [arXiv:1607.03540 \[gr-qc\]](#)
- [9] L. Bovard, D. Martin, F. Guercilena, A. Arcones, L. Rezzolla, and O. Korobkin, *Phys. Rev. D* **96**, 124005 (2017), [arXiv:1709.09630 \[gr-qc\]](#)
- [10] A. Perego, D. Radice, and S. Bernuzzi, *Astrophys. J. Lett.* **850**, L37 (2017), [arXiv:1711.03982 \[astro-ph.HE\]](#)
- [11] E. Annala, T. Gorda, A. Kurkela, and A. Vuorinen, *Phys. Rev. Lett.* **120**, 172703 (2018), [arXiv:1711.02644 \[astro-ph.HE\]](#)
- [12] A. Bauswein, O. Just, H.-T. Janka, and N. Stergioulas, *Astrophys. J. Lett.* **850**, L34 (2017), [arXiv:1710.06843 \[astro-ph.HE\]](#)
- [13] B. Margalit and B. D. Metzger, *Astrophys. J. Lett.* **850**, L19 (2017), [arXiv:1710.05938 \[astro-ph.HE\]](#)
- [14] D. Radice, A. Perego, F. Zappa, and S. Bernuzzi, *Astrophys. J. Lett.* **852**, L29 (2018), [arXiv:1711.03647 \[astro-ph.HE\]](#)
- [15] L. Rezzolla, E. R. Most, and L. R. Weih, *Astrophys. J. Lett.* **852**, L25 (2018), [arXiv:1711.00314 \[astro-ph.HE\]](#)
- [16] M. Ruiz, S. L. Shapiro, and A. Tsokaros, *Phys. Rev. D* **97**, 021501 (2018), [arXiv:1711.00473 \[astro-ph.HE\]](#)
- [17] M. Shibata, S. Fujibayashi, K. Hotokezaka, K. Kiuchi, K. Kyutoku, Y. Sekiguchi, and M. Tanaka, *Phys. Rev. D* **96**, 123012 (2017), [arXiv:1710.07579 \[astro-ph.HE\]](#)
- [18] E. R. Most, L. R. Weih, L. Rezzolla, and J. Schaffner-Bielich, *arxiv:1803.00549* (2018), [arXiv:1803.00549 \[gr-qc\]](#)
- [19] P. C. Peters, *Phys. Rev.* **136**, B1224 (1964)
- [20] E. A. Huerta *et al.*, *Phys. Rev. D* **95**, 024038 (2017), [arXiv:1609.05933 \[gr-qc\]](#)
- [21] E. A. Huerta, C. J. Moore, P. Kumar, D. George, A. J. K. Chua, R. Haas, E. Wessel, D. Johnson, D. Glennon, A. Rebei, A. M. Holgado, J. R. Gair, and H. P. Pfeiffer, *Phys. Rev. D* **97**, 024031 (2018), [arXiv:1711.06276 \[gr-qc\]](#)
- [22] H. Yang, W. E. East, V. Paschalidis, F. Pretorius, and R. F. P. Mendes, *arxiv:1806.00158* (2018), [arXiv:1806.00158 \[gr-qc\]](#)
- [23] P. C. Peters and J. Mathews, *Phys. Rev.* **131**, 435 (1963)
- [24] J. Samsing, M. MacLeod, and E. Ramirez-Ruiz, *Astrophys. J.* **846**, 36 (2017), [arXiv:1609.09114 \[astro-ph.HE\]](#)
- [25] C. L. Rodriguez, P. Amaro-Seoane, S. Chatterjee, and F. A. Rasio, *Phys. Rev. Lett.* **120**, 151101 (2018), [arXiv:1712.04937 \[astro-ph.HE\]](#)
- [26] M. Bonetti, A. Perego, P. R. Capelo, M. Dotti, and M. C. Miller, *Publications of the Astron. Soc. of Australia* **35**, e017 (2018), [arXiv:1801.03506 \[astro-ph.HE\]](#)
- [27] N. Ivanova, S. Justham, X. Chen, O. De Marco, C. L. Fryer, E. Gaburov, H. Ge, E. Glebbeek, Z. Han, X.-D. Li, G. Lu, T. Marsh, P. Podsiadlowski, A. Potter, N. Soker, R. Taam, T. M. Tauris, E. P. J. van den Heuvel, and R. F. Webbink, *Astronomy and Astrophysics Reviews* **21**, 59 (2013), [arXiv:1209.4302 \[astro-ph.HE\]](#)
- [28] D. Tsang, *Astrophys. J.* **777**, 103 (2013), [arXiv:1307.3554 \[astro-ph.HE\]](#)
- [29] W.-W. Tan, X.-L. Fan, and F. Y. Wang, *Mon. Not. R. Astron. Soc.* **475**, 1331 (2018), [arXiv:1712.04641 \[astro-ph.HE\]](#)
- [30] M. Punturo *et al.*, *Class. Quantum Grav.* **27**, 084007 (2010)
- [31] M. Punturo *et al.*, *Class. Quantum Grav.* **27**, 194002 (2010)
- [32] B. P. Abbott *et al.* (LIGO Scientific), *Class. Quant. Grav.* **34**, 044001 (2017), [arXiv:1607.08697 \[astro-ph.IM\]](#)
- [33] H. Miao, Y. Ma, C. Zhao, and Y. Chen, *Phys. Rev. Lett.* **115**, 211104 (2015), [arXiv:1506.00117 \[quant-ph\]](#)
- [34] H. Miao, H. Yang, and D. Martynov, *ArXiv e-prints* (2017), [arXiv:1712.07345 \[gr-qc\]](#)
- [35] C. Chirenti, R. Gold, and M. C. Miller, *Astrophys. J.* **837**, 67 (2017), [arXiv:1612.07097 \[astro-ph.HE\]](#)
- [36] S. Bose, K. Chakravarti, L. Rezzolla, B. S. Sathyaprakash, and K. Takami, *Phys. Rev. Lett.* **120**, 031102 (2018), [arXiv:1705.10850 \[gr-qc\]](#)
- [37] K. S. Tai, S. T. McWilliams, and F. Pretorius, *Phys. Rev. D* **90**, 103001 (2014), [arXiv:1403.7754 \[gr-qc\]](#)
- [38] L. Gondán, B. Kocsis, P. Raffai, and Z. Frei, *Astrophys. J.* **855**, 34 (2018), [arXiv:1705.10781 \[astro-ph.HE\]](#)
- [39] A. P. Ji, A. Frebel, A. Chiti, and J. D. Simon, *Nature* **531**, 610 (2016), [arXiv:1512.01558](#)
- [40] M. Turner, *Astrophys. J.* **216**, 914 (1977)
- [41] M. Turner, *Astrophys. J.* **216**, 610 (1977)
- [42] A. Parisi and R. Sturani, *Phys. Rev. D* **97**, 043015 (2018), [arXiv:1705.04751 \[gr-qc\]](#)
- [43] A. Bauswein and H.-T. Janka, *Phys. Rev. Lett.* **108**, 011101 (2012), [arXiv:1106.1616 \[astro-ph.SR\]](#)
- [44] N. Stergioulas, A. Bauswein, K. Zagkouris, and H.-T. Janka, *Mon. Not. R. Astron. Soc.* **418**, 427 (2011), [arXiv:1105.0368 \[gr-qc\]](#)
- [45] K. Takami, L. Rezzolla, and L. Baiotti, *Phys. Rev. Lett.* **113**, 091104 (2014), [arXiv:1403.5672 \[gr-qc\]](#)
- [46] K. Takami, L. Rezzolla, and L. Baiotti, *Phys. Rev. D* **91**, 064001 (2015), [arXiv:1412.3240 \[gr-qc\]](#)
- [47] S. Bernuzzi, T. Dietrich, and A. Nagar, *Phys. Rev. Lett.* **115**, 091101 (2015), [arXiv:1504.01764 \[gr-qc\]](#)
- [48] L. Rezzolla and K. Takami, *Phys. Rev. D* **93**, 124051 (2016), [arXiv:1604.00246 \[gr-qc\]](#)
- [49] B. C. Stephens, W. E. East, and F. Pretorius, *Astrophys. J.* **737**, L5 (2011), [arXiv:1105.3175 \[astro-ph.HE\]](#)
- [50] R. Gold, S. Bernuzzi, M. Thierfelder, B. Brügmann, and F. Pretorius, *Phys. Rev. D* **86**, 121501 (2012), [arXiv:1109.5128 \[gr-qc\]](#)
- [51] N. Moldenhauer, C. M. Markakis, N. K. Johnson-McDaniel, W. Tichy, and B. Brügmann, *Phys. Rev. D* **90**, 084043 (2014), [arXiv:1408.4136 \[gr-qc\]](#)
- [52] V. Paschalidis, W. E. East, F. Pretorius, and S. L. Shapiro, *Phys. Rev. D* **92**, 121502 (2015), [arXiv:1510.03432 \[astro-ph.HE\]](#)
- [53] W. E. East, V. Paschalidis, F. Pretorius, and S. L. Shapiro, *Phys. Rev. D* **93**, 024011 (2016), [arXiv:1511.01093 \[astro-ph.HE\]](#)
- [54] W. E. East, V. Paschalidis, and F. Pretorius, *Classical and Quantum Gravity* **33**, 244004 (2016), [arXiv:1609.00725 \[astro-ph.HE\]](#)
- [55] W. E. East, F. Pretorius, and B. C. Stephens, *Phys. Rev. D* **85**, 124009 (2012), [arXiv:1111.3055 \[astro-ph.HE\]](#)
- [56] L. Lehner, S. L. Liebling, C. Palenzuela, and P. M. Motl, *Phys. Rev. D* **94**, 043003 (2016), [arXiv:1605.02369 \[gr-qc\]](#)
- [57] D. Radice, S. Bernuzzi, and C. D. Ott, *Phys. Rev. D* **94**, 064011 (2016), [arXiv:1603.05726 \[gr-qc\]](#)
- [58] M. Hanauske, K. Takami, L. Bovard, L. Rezzolla, J. A. Font, F. Galeazzi, and H. Stöcker, *Phys. Rev. D* **96**, 043004 (2017), [arXiv:1611.07152 \[gr-qc\]](#)

- [59] D. Radice, F. Galeazzi, J. Lippuner, L. F. Roberts, C. D. Ott, and L. Rezzolla, *Mon. Not. R. Astron. Soc.* **460**, 3255 (2016), [arXiv:1601.02426 \[astro-ph.HE\]](#)
- [60] N. R. Tanvir, A. J. Levan, A. S. Fruchter, J. Hjorth, R. A. Hounsell, K. Wiersema, and R. L. Tunnicliffe, *Nature* **500**, 547 (2013), [arXiv:1306.4971 \[astro-ph.HE\]](#)
- [61] R. T. Wollaeger, O. Korobkin, C. J. Fontes, S. K. Rosswog, W. P. Even, C. L. Fryer, J. Sollerman, A. L. Hungerford, D. R. van Rossum, and A. B. Wollaber, *ArXiv e-prints* (2017), [arXiv:1705.07084 \[astro-ph.HE\]](#)
- [62] D. Grossman, O. Korobkin, S. Rosswog, and T. Piran, *Mon. Not. R. Astron. Soc.* **439**, 757 (2014), [arXiv:1307.2943 \[astro-ph.HE\]](#)
- [63] M. Alcubierre, *Introduction to 3+1 Numerical Relativity* (Oxford University Press, Oxford, UK, 2008)
- [64] L. Rezzolla and O. Zanotti, *Relativistic Hydrodynamics* (Oxford University Press, Oxford, UK, 2013)
- [65] D. Alic, C. Bona-Casas, C. Bona, L. Rezzolla, and C. Palenzuela, *Phys. Rev. D* **85**, 064040 (2012), [arXiv:1106.2254 \[gr-qc\]](#)
- [66] D. Alic, W. Kastaun, and L. Rezzolla, *Phys. Rev. D* **88**, 064049 (2013), [arXiv:1307.7391 \[gr-qc\]](#)
- [67] M. Bezares, C. Palenzuela, and C. Bona, *Phys. Rev. D* **95**, 124005 (2017), [arXiv:1705.01071 \[gr-qc\]](#)
- [68] M. Dumbser, F. Guercilena, S. Köppel, L. Rezzolla, and O. Zanotti, *Phys. Rev. D* **97**, 084053 (2018), [arXiv:1707.09910 \[gr-qc\]](#)
- [69] C. Bona, T. Ledvinka, C. Palenzuela, and M. Záček, *Phys. Rev. D* **67**, 104005 (2003), [gr-qc/0302083](#)
- [70] C. Bona, T. Ledvinka, C. Palenzuela, and M. Záček, *Phys. Rev. D* **69**, 064036 (2004), [gr-qc/0307067](#)
- [71] D. Alic, C. Bona, and C. Bona-Casas, *Phys. Rev. D* **79**, 044026 (2009), [arXiv:0811.1691 \[gr-qc\]](#)
- [72] A. Dedner, F. Kemm, D. Kröner, C. D. Munz, T. Schnitzer, and M. Wesenberg, *Journal of Computational Physics* **175**, 645 (2002)
- [73] M. Shibata and T. Nakamura, *Phys. Rev. D* **52**, 5428 (1995)
- [74] T. W. Baumgarte and S. L. Shapiro, *Phys. Rev. D* **59**, 024007 (1999), [gr-qc/9810065](#)
- [75] T. W. Baumgarte and S. L. Shapiro, *Numerical Relativity: Solving Einstein's Equations on the Computer* (Cambridge University Press, Cambridge, UK, 2010)
- [76] D. Brown, P. Diener, O. Sarbach, E. Schnetter, and M. Tiglio, *Phys. Rev. D* **79**, 044023 (2009), [arXiv:0809.3533 \[gr-qc\]](#)
- [77] F. Löffler, J. Faber, E. Bentivegna, T. Bode, P. Diener, R. Haas, I. Hinder, B. C. Mundim, C. D. Ott, E. Schnetter, G. Allen, M. Campanelli, and P. Laguna, *Class. Quantum Grav.* **29**, 115001 (2012), [arXiv:1111.3344 \[gr-qc\]](#)
- [78] H. O. Kreiss and J. Olinger, *Methods for the approximate solution of time dependent problems* (GARP publication series No. 10, Geneva, 1973)
- [79] F. Banyuls, J. A. Font, J. M. Ibáñez, J. M. Martí, and J. A. Miralles, *Astrophys. J.* **476**, 221 (1997)
- [80] D. Radice, L. Rezzolla, and F. Galeazzi, *Mon. Not. R. Astron. Soc. L.* **437**, L46 (2014), [arXiv:1306.6052 \[gr-qc\]](#)
- [81] D. Radice, L. Rezzolla, and F. Galeazzi, *Class. Quantum Grav.* **31**, 075012 (2014), [arXiv:1312.5004 \[gr-qc\]](#)
- [82] D. Radice, L. Rezzolla, and F. Galeazzi, in *Numerical Modeling of Space Plasma Flows ASTRONUM-2014*, Astronomical Society of the Pacific Conference Series, Vol. 498, edited by N. V. Pogorelov, E. Audit, and G. P. Zank (2015) p. 121, [arXiv:1502.00551 \[gr-qc\]](#)
- [83] A. Suresh and H. T. Huynh, *Journal of Computational Physics* **136**, 83 (1997)
- [84] D. Radice and L. Rezzolla, *Astron. Astrophys.* **547**, A26 (2012), [arXiv:1206.6502 \[astro-ph.IM\]](#)
- [85] A. Harten, P. D. Lax, and B. van Leer, *SIAM Rev.* **25**, 35 (1983)
- [86] X. Y. Hu, N. A. Adams, and C.-W. Shu, *Journal of Computational Physics* **242**, 169 (2013), [arXiv:1203.1540 \[physics.flu-dyn\]](#)
- [87] M. J. Berger and P. Colella, *J. Comput. Phys.* **82**, 64 (1989)
- [88] K. A. van Riper and J. M. Lattimer, *Astrophys. J.* **249**, 270 (1981)
- [89] M. Ruffert, H.-T. Janka, K. Takahashi, and G. Schaefer, *Astron. Astrophys.* **319**, 122 (1997), [astro-ph/9606181](#)
- [90] S. Rosswog, E. Ramirez-Ruiz, and M. B. Davies, *Mon. Not. R. Astron. Soc.* **345**, 1077 (2003), [arXiv:astro-ph/0110180](#)
- [91] E. O'Connor and C. D. Ott, *Class. Quantum Grav.* **27**, 114103 (2010), [arXiv:0912.2393 \[astro-ph.HE\]](#)
- [92] A. Perego, S. Rosswog, R. M. Cabezón, O. Korobkin, R. Käppeli, A. Arcones, and M. Liebendörfer, *Mon. Not. R. Astron. Soc.* **443**, 3134 (2014), [arXiv:1405.6730 \[astro-ph.HE\]](#)
- [93] F. Galeazzi, W. Kastaun, L. Rezzolla, and J. A. Font, *Phys. Rev. D* **88**, 064009 (2013), [arXiv:1306.4953 \[gr-qc\]](#)
- [94] W. Kastaun, F. Galeazzi, D. Alic, L. Rezzolla, and J. A. Font, *Phys. Rev. D* **88**, 021501 (2013), [arXiv:1301.7348 \[gr-qc\]](#)
- [95] S. Bernuzzi, T. Dietrich, W. Tichy, and B. Brügmann, *Phys. Rev. D* **89**, 104021 (2014), [arXiv:1311.4443 \[gr-qc\]](#)
- [96] S. Typel, G. Röpke, T. Klähn, D. Blaschke, and H. H. Wolter, *Phys. Rev. C* **81**, 015803 (2010), [arXiv:0908.2344 \[nucl-th\]](#)
- [97] J. M. Lattimer and F. D. Swesty, *Nucl. Phys. A* **535**, 331 (1991)
- [98] P. B. Demorest, T. Pennucci, S. M. Ransom, M. S. E. Roberts, and J. W. T. Hessels, *Nature* **467**, 1081 (2010), [arXiv:1010.5788 \[astro-ph.HE\]](#)
- [99] J. Antoniadis, P. C. C. Freire, N. Wex, T. M. Tauris, R. S. Lynch, and et al., *Science* **340**, 448 (2013), [arXiv:1304.6875 \[astro-ph.HE\]](#)
- [100] I. Tews, J. M. Lattimer, A. Ohnishi, and E. E. Kolomeitsev, *Astrophys. J.* **848**, 105 (2017), [arXiv:1611.07133 \[nucl-th\]](#)
- [101] E. Schnetter, S. H. Hawley, and I. Hawke, *Class. Quantum Grav.* **21**, 1465 (2004), [gr-qc/0310042](#)
- [102] W. Kastaun and F. Galeazzi, *Phys. Rev. D* **91**, 064027 (2015), [arXiv:1411.7975 \[gr-qc\]](#)
- [103] L. Bovard and L. Rezzolla, *Classical and Quantum Gravity* **34**, 215005 (2017), [arXiv:1705.07882](#)
- [104] S. Wanajo, Y. Sekiguchi, N. Nishimura, K. Kiuchi, K. Kyutoku, and M. Shibata, *Astrophys. J.* **789**, L39 (2014), [arXiv:1402.7317 \[astro-ph.SR\]](#)
- [105] W. Kastaun, R. Ciolfi, and B. Giacomazzo, *Phys. Rev. D* **94**, 044060 (2016), [arXiv:1607.02186 \[astro-ph.HE\]](#)
- [106] V. Mewes, F. Galeazzi, J. A. Font, P. J. Montero, and N. Stergioulas, *Mon. Not. R. Astron. Soc.* **461**, 2480 (2016), [arXiv:1605.02629 \[astro-ph.HE\]](#)
- [107] J. Lippuner and L. F. Roberts, *Astrophys. J., Supp.* **233**, 18 (2017), [arXiv:1706.06198 \[astro-ph.HE\]](#)
- [108] R. H. Cyburt, A. M. Amthor, R. Ferguson, Z. Meisel, K. Smith, S. Warren, A. Heger, R. D. Hoffman, T. Rauscher, A. Sakharuk, H. Schatz, F. K. Thielemann, and M. Wiescher, *Astrophys. J., Supp.* **189**, 240 (2010)
- [109] I. V. Panov, I. Y. Korneev, T. Rauscher, G. Martínez-Pinedo, A. Kelić-Heil, N. T. Zinner, and F.-K. Thielemann, *Astron. Astrophys.* **513**, A61 (2010)
- [110] L. F. Roberts, D. Kasen, W. H. Lee, and E. Ramirez-Ruiz, *Astrophys. J. Lett.* **736**, L21 (2011), [arXiv:1104.5504 \[astro-ph.HE\]](#)

- [111] G. M. Fuller, W. A. Fowler, and M. J. Newman, *Astrophys. J., Supp.* **48**, 279 (1982)
- [112] S.-i. Fujimoto, N. Nishimura, and M.-a. Hashimoto, *Astrophys. J.* **680**, 1350-1358 (2008), arXiv:0804.0969
- [113] O. Korobkin, S. Rosswog, A. Arcones, and C. Winteler, *Mon. Not. R. Astron. Soc.* **426**, 1940 (2012), arXiv:1206.2379 [astro-ph.SR]
- [114] F. Timmes and D. Arnett, *Astrophysical Journal, Supplement Series* **125**, 277 (1999)
- [115] F. X. Timmes and F. D. Swesty, *Astrophys. J., Supp.* **126**, 501 (2000)
- [116] E. T. Newman and R. Penrose, *J. Math. Phys.* **3**, 566 (1962), erratum in *J. Math. Phys.* **4**, 998 (1963)
- [117] N. T. Bishop and L. Rezzolla, *Living Reviews in Relativity* **19**, 2 (2016), arXiv:1606.02532 [gr-qc]
- [118] J. N. Goldberg, A. J. MacFarlane, E. T. Newman, F. Rohrlich, and E. C. G. Sudarshan, *J. Math. Phys.* **8**, 2155 (1967)
- [119] C. Reisswig and D. Pollney, *Class. Quantum Grav.* **28**, 195015 (2011), arXiv:1006.1632 [gr-qc]
- [120] W. H. Lee, E. Ramirez-Ruiz, and G. van de Ven, *Astrophys. J.* **720**, 953 (2010), arXiv:0909.2884 [astro-ph.HE]
- [121] T. A. Thompson, *Astrophys. J.* **741**, 82 (2011), arXiv:1011.4322 [astro-ph.HE]
- [122] R. M. O'Leary, B. Kocsis, and A. Loeb, *Mon. Not. R. Astron. Soc.* **395**, 2127 (2009), arXiv:0807.2638
- [123] B. Kocsis and J. Levin, *Phys. Rev. D* **85**, 123005 (2012), arXiv:1109.4170 [astro-ph.CO]
- [124] F. Antonini and H. B. Perets, *Astrophys. J.* **757**, 27 (2012), arXiv:1203.2938
- [125] C. Breu and L. Rezzolla, *Mon. Not. R. Astron. Soc.* **459**, 646 (2016), arXiv:1601.06083 [gr-qc]
- [126] L. R. Weih, E. R. Most, and L. Rezzolla, *Mon. Not. R. Astron. Soc.* **473**, L126 (2018), arXiv:1709.06058 [gr-qc]
- [127] R. Gold and B. Brügmann, *Phys. Rev. D* **88**, 064051 (2013), arXiv:1209.4085 [gr-qc]
- [128] W. E. East and F. Pretorius, *Astrophys. J.* **760**, L4 (2012), arXiv:1208.5279 [astro-ph.HE]
- [129] F. Foucart, R. Haas, M. D. Duez, E. O'Connor, C. D. Ott, L. Roberts, L. E. Kidder, J. Lippuner, H. P. Pfeiffer, and M. A. Scheel, *Phys. Rev. D* **93**, 044019 (2016), arXiv:1510.06398 [astro-ph.HE]
- [130] F. Foucart, M. Chandra, C. F. Gammie, and E. Quataert, *Mon. Not. R. Astron. Soc.* **456**, 1332 (2016), arXiv:1511.04445 [astro-ph.HE]
- [131] Y. Sekiguchi, K. Kiuchi, K. Kyutoku, and M. Shibata, *Phys. Rev. D* **91**, 064059 (2015), arXiv:1502.06660 [astro-ph.HE]
- [132] F. Foucart, E. O'Connor, L. Roberts, L. E. Kidder, H. P. Pfeiffer, and M. A. Scheel, *Phys. Rev. D* **94**, 123016 (2016), arXiv:1607.07450 [astro-ph.HE]
- [133] Y. Sekiguchi, K. Kiuchi, K. Kyutoku, M. Shibata, and K. Taniguchi, *Phys. Rev. D* **93**, 124046 (2016), arXiv:1603.01918 [astro-ph.HE]
- [134] W. E. East, S. T. McWilliams, J. Levin, and F. Pretorius, *Phys. Rev. D* **87**, 043004 (2013), arXiv:1212.0837 [gr-qc]
- [135] C. Palenzuela, S. L. Liebling, D. Neilsen, L. Lehner, O. L. Caballero, E. O'Connor, and M. Anderson, *Phys. Rev. D* **92**, 044045 (2015), arXiv:1505.01607 [gr-qc]
- [136] C. Messenger, K. Takami, S. Gossan, L. Rezzolla, and B. S. Sathyaprakash, *Phys. Rev. X* **4**, 041004 (2014)
- [137] L. Dessart, C. D. Ott, A. Burrows, S. Rosswog, and E. Livne, *Astrophys. J.* **690**, 1681 (2009), arXiv:0806.4380
- [138] R. Fernández and B. D. Metzger, *Mon. Not. R. Astron. Soc.* **435**, 502 (2013), arXiv:1304.6720 [astro-ph.HE]
- [139] R. Fernández, D. Kasen, B. D. Metzger, and E. Quataert, *Mon. Not. R. Astron. Soc.* **446**, 750 (2015), arXiv:1409.4426 [astro-ph.HE]
- [140] D. M. Siegel, R. Ciolfi, and L. Rezzolla, *Astrophys. J.* **785**, L6 (2014), arXiv:1401.4544 [astro-ph.HE]
- [141] B. D. Metzger and R. Fernández, *Mon. Not. R. Astron. Soc.* **441**, 3444 (2014), arXiv:1402.4803 [astro-ph.HE]
- [142] L. Rezzolla and P. Kumar, *Astrophys. J.* **802**, 95 (2015), arXiv:1410.8560 [astro-ph.HE]
- [143] R. Ciolfi and D. M. Siegel, *Astrophys. J.* **798**, L36 (2015), arXiv:1411.2015 [astro-ph.HE]
- [144] O. Just, A. Bauswein, R. A. Pulpillo, S. Goriely, and H.-T. Janka, *Mon. Not. R. Astron. Soc.* **448**, 541 (2015), arXiv:1406.2687 [astro-ph.SR]
- [145] D. Martin, A. Perego, A. Arcones, F.-K. Thielemann, O. Korobkin, and S. Rosswog, *Astrophys. J.* **813**, 2 (2015), arXiv:1506.05048 [astro-ph.SR]
- [146] K. Kiuchi, P. Cerdá-Durán, K. Kyutoku, Y. Sekiguchi, and M. Shibata, *Phys. Rev. D* **92**, 124034 (2015), arXiv:1509.09205 [astro-ph.HE]